

Secondary atomization of viscoelastic fluid

Dissertation submitted in partial fulfilment of the requirements
for the award of the degree of

Master of Technology

by

Denish Lakhani

(Roll No. 23M0027)

Under the Supervision of

Prof. Hrishikesh Gadgil



Aerospace Engineering

Department of Aerospace Engineering

INDIAN INSTITUTE OF TECHNOLOGY BOMBAY

Mumbai - 400076, India

May, 2025

Thesis Approval sheet

This dissertation entitled **Secondary atomization of viscoelastic fluid** by **Denish Lakhani**, Roll No. 23M0027, is approved for the degree of **Master of Technology** from the Indian Institute of Technology Bombay.

Digital Signature
V R Kowsik BODI (i11093)
26-Jun-25 11:25:58 AM

.....
Prof. Kowsik Bodi
(Examiner 1)

Digital Signature
Neeraj Kumbhakarna (i14285)
25-Jun-25 05:59:19 PM

.....
Prof. Neeraj Kumbhakarna
(Examiner 2)

Digital Signature
Hrishikesh Gadgil (i15116)
27-Jun-25 10:58:39 PM

.....
Prof. Hrishikesh Gadgil
(Guide)

Date: 28/06/2025

Place: Navsari

Declaration

I hereby declare that the content presented in this dissertation is the result of my own independent work and investigation. Wherever ideas, data, or text from other sources have been used, they have been clearly acknowledged and appropriately cited. I affirm that I have maintained the highest standards of academic integrity and have neither engaged in plagiarism nor misrepresented any information, data, or source.

I understand that any breach of academic ethics may attract disciplinary action as per the rules of the Institute and could also lead to legal consequences from the rightful owner of the misrepresented or improperly cited material.

Denish
.....

Denish Lakhani

Roll No.: 23M0027

Date: 29/05/2025

Place: IIT Bombay

CERTIFICATE

Certified that this M.Tech Stage II project Report titled "Secondary atomization of non-Newtonian liquid" by Denish Lakhani is approved by me for submission. Certified further that, to the best of my knowledge, the report represents work carried out by the student.

Date: 29 May 2025


Prof. Hrishikesh Gadgil

ACKNOWLEDGMENT

I would like to express my gratitude and respect to Prof. Hrishikesh Gadgil, my guide in this M.Tech Stage II project, for the guidance and supervision he has provided me in the successful completion of the seminar work. In addition to general guidance, he has often provided in-depth technical feedback to various doubts and problems faced by me during this seminar and for this I would like to express my sincere appreciations.

Denish Lakhani

Date: 29 May 2025

Indian Institute of technology, Bombay

ABSTRACT

Secondary atomization of non-Newtonian fluids plays a critical role in various industrial applications, including fuel sprays and coating processes. This study investigates the dynamics and mechanisms underlying the secondary atomization of non-Newtonian fluids, characterized by their complex flow behavior and viscosity-dependent properties. Using an experimental techniques, we analyze the impact of fluid rheology, flow conditions, and atomization parameters on droplet size distribution and spray characteristics. Our findings reveal that the non-Newtonian nature of the fluid significantly influences the atomization process, leading to distinct droplet formation patterns compared to Newtonian fluids. The study provides insights into optimizing atomization processes for improved performance and efficiency in practical applications. The results highlight the importance of considering fluid rheology in the design and operation of atomization systems.

Contents

1	INTRODUCTION	1
1.1	Objective	4
2	LITERATURE REVIEW	5
2.1	Experimental study	6
2.2	Property of non-newtonian fluid	10
2.3	Aerodynamic breakup of the droplet	12
2.4	Numerical study on shear-thinning droplet atomization	15
2.5	Regime map	16
2.6	Summary	18
3	Experimental setup	19
3.1	Preparation of gel	20
3.2	Rheological properties of gel	21
3.2.1	Shear thinning	21
3.2.2	Visco-elasticity	23
3.3	Experimental test conditions	23
3.4	Property calculation	24
3.5	Image analysis and data processing	26
4	Results and discussion	30
4.1	Bag breakup mode	33
4.2	Bag breakup morphology and regime classification	35
4.3	Regime map	40
4.4	Hole rim destabilization	42
4.5	Hole merging	43
4.6	Deformation behavior of droplets – streamwise and cross-streamwise . . .	44
4.7	Initiation time	48
5	CONCLUSION	50
5.1	Future work	51
	REFERENCES	52

List of Figures

1.1	Atomization process ^[1]	1
1.2	Types of fluid ^[2]	2
2.1	Modes of breakup ^[1]	7
2.2	Schematic representation of stages in bag breakup ^[1]	13
2.3	Regime map showing Weber number (We) vs Ohnesorge number (Oh) for various liquids including shear-thinning glycerol–water mixtures. ^[3]	17
3.1	Schematic diagram of the experimental setup.	19
3.2	Schematic diagram of the experimental setup.	22
3.3	Droplet dimension	26
3.4	Set the scale in imagej software	27
3.5	Image processing in ImageJ software	27
3.6	Generation of bag (We 18.4)	28
3.7	L/D_0 and $2H/D_0$ vs T (We 18.4)	29
4.1	Capillary breakup elongation	30
4.2	Minimum neck diameter h_{\min}/d_n as a function of time $(t - t_c)$ for a 3% HPMC solution. The data is fitted with a power-law model in the inertia-capillary regime and an exponential model in the elasto-capillary regime.	31
4.3	Comparison of normalized minimum neck diameter (h_{\min}/d_n) as a function of $(t - t_c)$ for 3%, 4%, and 5% HPMC solutions. The early-time behavior for all concentrations follows inertia-capillary thinning with a power-law decay ($B \approx 2/3$), while the late-time behavior shows exponential decay due to viscoelastic effects. Increasing polymer concentration leads to slower thinning and higher relaxation times, indicating stronger viscoelasticity.	32
4.4	Time-resolved droplet evolution of 3% HPMC solution at $We = 23.04$, depicting key breakup stages: deformation, bag inflation, bag film breakup, and main rim breakup.	33
4.5	Temporal evolution of normalized lateral width L/D_0 for three different HPMC concentrations under varying Weber numbers.	34
4.6	Temporal evolution of bag, bag-stamen, and multi-bag breakup for 3% HPMC droplets at different Weber numbers.	37

4.7	Temporal evolution of bag, bag-stamen, and multi-bag breakup for 4% HPMC droplets at different Weber numbers.	38
4.8	Temporal evolution of bag, bag-stamen, and multi-bag breakup for 5% HPMC droplets at different Weber numbers.	39
4.9	Regime map showing Weber number (We) versus Ohnesorge number (Oh) for ethanol and HPMC solutions at varying concentrations. Different breakup modes are identified across the fluid types.	40
4.10	Regime map representing the variation of breakup modes with Weber number and Elasticity number for different HPMC concentrations and ethanol.	41
4.11	Temporal variation of L/D_o for different Weber numbers and HPMC concentrations in the streamwise direction.	46
4.12	Temporal variation of $2H/D_o$ for different We and HPMC concentrations in the cross-streamwise direction.	47
4.13	Variation of initiation time $T_i = \frac{t}{t^*}$ with Weber number for various Newtonian and non-Newtonian fluids.	48

List of Tables

2.1	Non-dimensional numbers in secondary atomization	5
2.2	Breakup regimes of ethanol droplets at different Weber number ranges . .	9
2.3	Breakup regimes for different Newtonian fluids as a function of Weber number (We). ^[4,5]	9
3.1	Ethanol-HPMC composition (in % weight). ^[6]	21
3.2	Process parameter used in the present study	25
3.3	Measured Parameters	27
4.1	Weber number ranges corresponding to breakup regimes for different HPMC concentrations.	35

NOMENCLATURE

HPMC : Hydroxypropyl methylcellulose
We : Weber number
Oh : Ohnesorge numbe
 t^* : Characteristic time
 t_0 : Initiation time
T : Non-dimensional time
 D_0 : Initial diameter
RT : Rayleigh-Taylor
KH : Kelvin-Helmholtz
ROI : Region of intrest
SW : Streamwise
CS : Cross stream wise
Bo : Bond number
 u_r : Receding velocity
 a_r : Acceleration experienced by the receding rim
 σ : Surface tension
 δ : Thickness of the bag film
 ρ_l : Liquid density

Chapter 1

INTRODUCTION

The atomization of liquids plays a vital role in several engineering and industrial processes such as fuel injection in combustion [1], spray cooling, agricultural spraying, pharmaceutical applications, and more. Atomization, in simple terms, refers to the process where a liquid is broken up into smaller droplets. This process generally occurs in two main stages: primary atomization, where the liquid jet or sheet initially breaks into large droplets or ligaments, and secondary atomization, where these larger droplets undergo further breakup due to interaction with the surrounding gas phase.

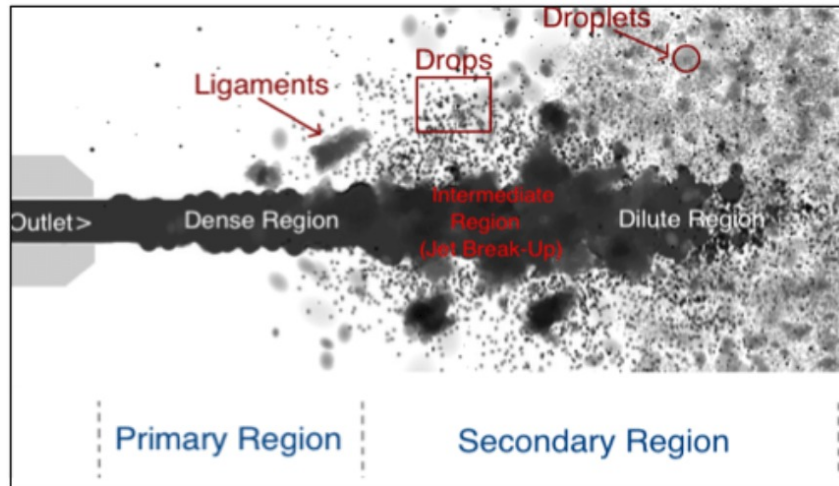


Figure 1.1: Atomization process^[1]

While a significant amount of research has been carried out on the atomization of Newtonian fluids like water or kerosene, the behavior of non-Newtonian fluids in similar conditions is less understood. Non-Newtonian fluids, unlike Newtonian ones, exhibit complex rheological behavior—where viscosity is not constant but depends on the applied shear rate. Some also possess yield stress, meaning they behave like solids until a critical stress is exceeded. This makes their atomization characteristics distinctly different, and often more complicated.

In recent years, there has been a growing interest in using gel propellants in aerospace applications. These propellants exhibit non-Newtonian characteristics and offer several advantages such as improved safety, storability, and controllable combustion. However, for their efficient use in propulsion systems, a deep understanding of their atomization behavior—especially during the secondary atomization stage is essential. Inadequate breakup can lead to poor mixing and incomplete combustion, affecting overall system

efficiency.

Non-Newtonian fluids are categorized based on how their viscosity changes with shear rate. The three most commonly studied types include:

- **Shear-thinning fluids**(pseudoplastics) where viscosity decreases with increasing shear rate. Examples: blood, ketchup, paints.
- **Shear-thickening fluids** (dilatants), where viscosity increases with shear rate. Example: cornstarch in water.
- **Yield-stress fluids**, which behave like solids until a certain stress is applied. Examples: toothpaste, gels, some propellants.

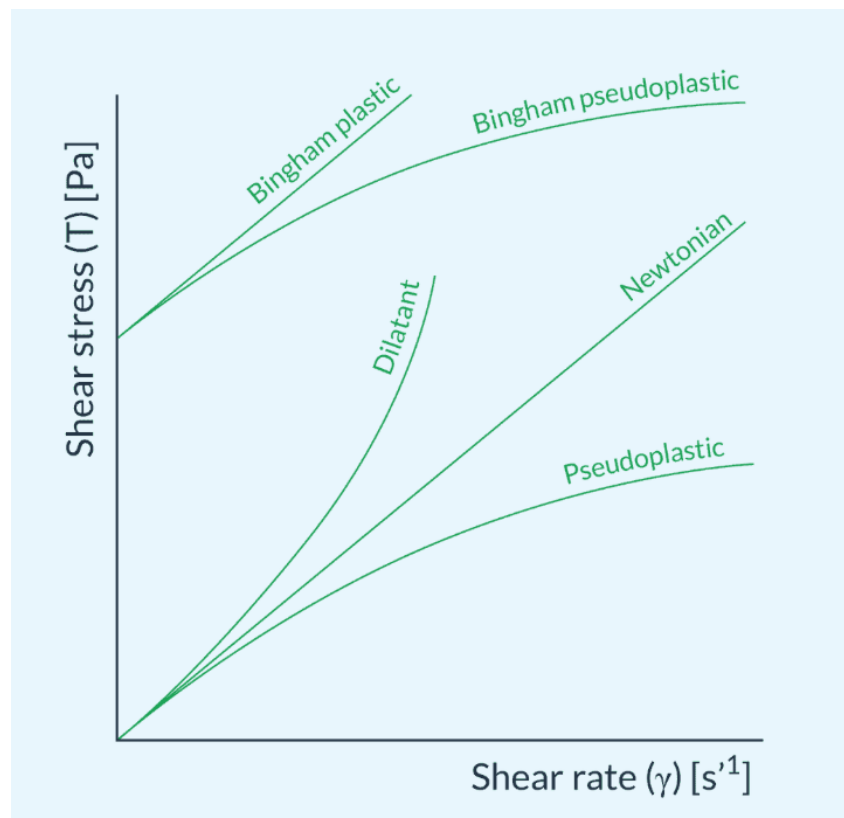


Figure 1.2: Types of fluid^[2]

In aerospace and defense systems, gelled fuels are a key area of interest. These fuels combine the advantages of both solid and liquid fuels but pose challenges in atomization due to their complex rheology. As the droplet of a non-Newtonian fluid moves through

a high-speed gas stream, it undergoes deformation and, depending on the acting forces, may or may not break up efficiently. This behavior is heavily influenced by the viscosity profile, elasticity, and stress of the fluid.

In the case of Newtonian fluids, researchers have identified distinct secondary breakup regimes depending on the (We) , which is the ratio of aerodynamic forces to surface tension. These regimes include:

- **Vibrational breakup**
- **Bag breakup**
- **Bag-and-stamen breakup**
- **Multi-Bag breakup**
- **Shear stripping**

For non-Newtonian fluids, however, these regimes apply or may appear modified. Additional parameters such as viscoelasticity, relaxation time, and yield stress come into play. The fluid's resistance to deformation can delay or completely suppress the breakup process, leading to larger droplet sizes and potentially uneven spray patterns. This deviation from Newtonian behavior is critical for designing injectors and predicting spray performance.

To fully understand the atomization process in such fluids, researchers rely on several dimensionless numbers:

- **Weber number (We):** Compares aerodynamic force to surface tension.
- **Reynolds number (Re):** Compares inertial forces to viscous forces.
- **Ohnesorge number (Oh):** Describes the relative importance of viscosity.

In non-Newtonian flows, one may also consider generalized Reynolds numbers or use models like the **Herschel–Bulkley model**^[7] to capture the fluid's behavior.

1.1 Objective

The main objective of this project is to investigate the secondary atomization of non-Newtonian fluids, focusing on how their rheological properties influence droplet deformation and breakup under gas crossflow. The project aims to answer key questions such as:

- To understand yield stress influence droplet stability and breakup timing.
- Viscoelastic effects inhibit or enhance secondary atomization
- Shear-thinning behavior change the nature of ligament formation

To address these, the work involves a combination of rheological characterization, high-speed imaging of droplet breakup, and analysis of breakup modes under varying flow conditions. Insights from this study are expected to contribute to the development of more accurate atomization models tailored for non-Newtonian fluids and support better injector design for gel propellants.

Understanding the atomization behavior of non-Newtonian fluids is essential not only in aerospace but also in many fields where fluid spraying is a key process. In gelled propulsion systems, it directly impacts combustion efficiency and thrust control. In industrial spraying, it helps in achieving uniform coatings. Despite its importance, the literature on secondary breakup of such fluids is still limited, and more experimental data is needed to validate and develop theoretical models.

This study seeks to bridge that gap by systematically investigating the breakup mechanisms and identifying the key governing parameters. The outcomes could serve as a useful reference for future research in multiphase flow, fluid mechanics, and aerospace propulsion systems.

Chapter 2

LITERATURE REVIEW

Atomization, the process of disintegration of liquid masses into fine droplets, is a crucial mechanism in several industrial and scientific applications ranging from spray combustion, agricultural spraying, inkjet printing to medical diagnostics. Within this broad field, secondary atomization refers to the breakup of an already-formed droplet into smaller fragments when subjected to aerodynamic forces. While Newtonian fluids have been extensively studied in this context, non-Newtonian fluids, characterized by complex rheological behaviors such as shear-thinning, viscoelasticity, or yield stress, remain an active area of research.

Initial investigations into droplet breakup began in the early 20th century, primarily focusing on Newtonian fluids. These studies identified distinct breakup regimes: vibrational, bag, multimode, shear-induced, and catastrophic, primarily based on the Weber number (We), which compares aerodynamic to surface tension forces. Hinze (1955) [8] provided one of the foundational models explaining turbulent breakup of drops. The analysis was rooted in linear stability theory and served as a benchmark for later works.

Non-dimensional numbers emerge from the ratio of competing physical effects and are fundamental tools in fluid dynamics and multiphase flow analysis. [9,10] These parameters provide insight into the dominant forces governing a system without being confined to specific dimensional scales. By reducing the number of independent variables, they simplify complex problems and facilitate the generalization of experimental results across a range of conditions. Furthermore, such numbers allow for the compact representation of experimental data and help establish scalable correlations between physical phenomena.

Number	Expression	Ratio of physical factor
Reynolds number (Re)	$\frac{\rho_a U_0 d_0}{\mu_a}$	Inertia to viscous force
Weber number (We)	$\frac{\rho_a U_0^2 d_0}{\sigma}$	Aerodynamics to surface tension force
Ohnesorge number (Oh)	$\frac{\mu_a}{\sqrt{\rho_l \sigma d_0}}$	Viscous to surface tension force
Bond number (Bo)	$\frac{\Delta \rho g L^2}{\sigma}$	Gravity to surface tension force
Density ratio (ϵ)	$\frac{\rho_l}{\rho_a}$	Liquid to gas inertia
Viscosity ratio (N)	$\frac{\mu_l}{\mu_a}$	Liquid to gas viscosity

Table 2.1: Non-dimensional numbers in secondary atomization

In the context of secondary atomization, several dimensionless numbers play a pivotal role. Table 2.1 summarizes the key non-dimensional groups relevant to this regime. The interplay between aerodynamic and surface tension forces largely governs the breakup behavior of droplets. The Weber number (We), defined as the ratio of inertial to surface tension forces, is particularly important in identifying the threshold and modes of droplet disintegration.

Similarly, the Ohnesorge number (Oh), which incorporates the effect of liquid viscosity relative to inertial and surface tension forces, becomes significant in characterizing viscous damping during droplet deformation and fragmentation. In scenarios where gravitational effects are non-negligible—especially for larger droplets or in low-velocity flows—the Bond number (Bo) quantifies the competition between gravitational and surface tension forces.

In high-temperature or high-pressure environments such as combustion chambers, propulsion systems, or turbine engines, property gradients between phases become pronounced. Under such conditions, the density ratio and viscosity ratio (typically defined as the ratio of gas to liquid density and viscosity, respectively) become critical in governing droplet dynamics and the interfacial stress distribution.

2.1 Experimental study

Fluids can be broadly classified into Newtonian and non-Newtonian categories based on their flow behavior under applied stress. Newtonian fluids, such as water, air, alcohol, glycerol, and light motor oil, are characterized by their adherence to Newton’s law of viscosity, where the shear stress is linearly proportional to the rate of strain (velocity gradient). This relationship implies a constant viscosity regardless of the applied shear rate.

$$\tau = \mu \frac{du}{dy}$$

$$\tau = \text{Shear stress}$$

$$\mu = \text{Viscosity}$$

$$\frac{du}{dy} = \text{Velocity gradient}$$

In contrast, Non-Newtonian fluids, including custard, toothpaste, starch suspensions, cornstarch, paint, blood, melted butter, and shampoo, exhibit a more complex response, as their viscosity changes with varying shear rates, indicating they do not follow Newton’s

law of viscosity. This fundamental distinction plays a crucial role in understanding and modeling fluid behavior in various engineering applications.

In earlier studies, the behavior of non-Newtonian fluids was primarily analyzed using basic rheological measurements and visual observations of flow behavior under controlled conditions. Over time, more advanced experimental techniques have been introduced to gain deeper insights into their complex flow characteristics. Common methods used to analyze non-Newtonian fluids include rheometry for shear and viscoelastic properties, high-speed imaging for observing droplet impact and breakup, particle image velocimetry (PIV) for internal flow mapping, and laser-induced fluorescence (LIF) for tracking mixing and interface dynamics. Among these, high-speed imaging is widely considered the easiest and most accessible method, especially for analyzing droplet deformation, impact, and atomization. It provides direct visual evidence of transient fluid behavior and does not require complex setups or invasive probes. Its main advantages are ease of implementation, cost-effectiveness, and the ability to capture qualitative and quantitative data such as droplet size, shape evolution, and breakup timing in real time.

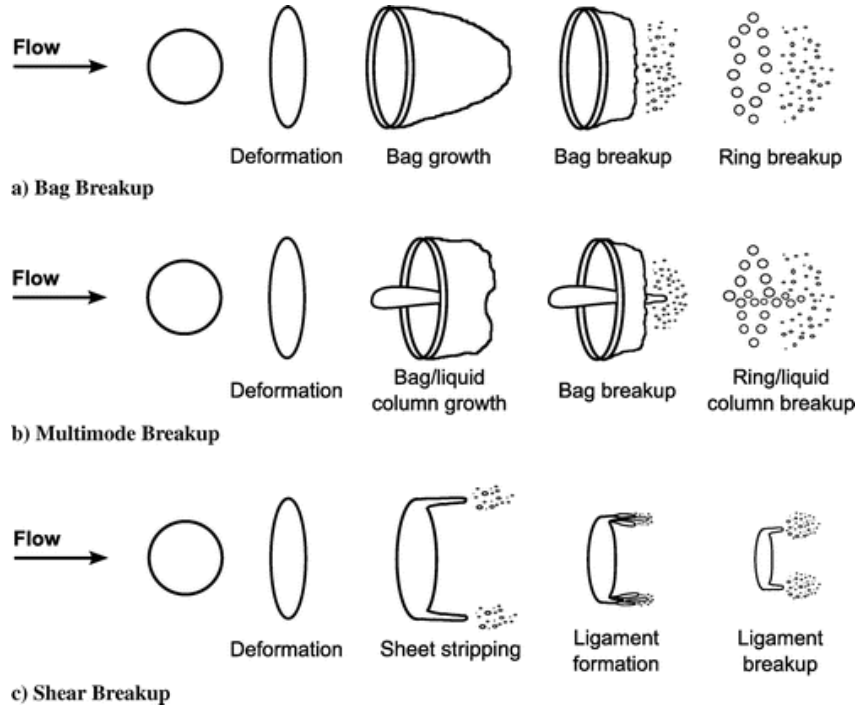


Figure 2.1: Modes of breakup^[1]

Droplet deformation refers to the alteration of a droplet's shape under the influence of aerodynamic forces encountered during its motion through a gaseous medium. A critical parameter governing this deformation is the Weber number (We), which quantifies the ratio of inertial forces to surface tension forces acting on the droplet. As observed experimentally, different ranges of the Weber number correspond to distinct breakup regimes.

In particular, Figure 2.1 illustrates how the breakup morphology evolves with increasing Weber number, transitioning through a series of well-defined stages.

Once a droplet enters the air stream, it is subjected to a rapid acceleration that disrupts the symmetry of pressure across its surface, causing it to deviate from its initial spherical shape. At relatively low Weber numbers, the droplet may undergo oscillatory motion due to surface disturbances that grow with time. These oscillations are driven by the relative motion between the droplet and the surrounding air, and their growth can eventually lead to surface instabilities. If these disturbances reach sufficient amplitude, the droplet fragments into smaller portions, often producing secondary droplets comparable in size to the original one. As the Weber number increases further, the breakup regime shifts, leading to more complex morphologies such as bag formation, sheet fragmentation, or catastrophic disintegration, depending on the flow conditions and fluid properties.

Early studies on Newtonian fluids such as ethanol suggest distinct breakup regimes as the Weber number increases.^[11] Due to its relatively low viscosity and surface tension, ethanol serves as a representative fluid for examining droplet breakup under aerodynamic forces. At low Weber numbers ($We < 12$),^[12] the droplet maintains its integrity while undergoing surface oscillations—this is referred to as the vibrational regime. As the Weber number increases to the intermediate range ($12 \leq We < 50$), surface tension is no longer sufficient to stabilize the droplet, leading to the formation of a thin membrane supported by a rim, known as the bag breakup regime. In the range of ($50 \leq We < 100$), the bag-stamen regime is observed, where the bag forms along with a trailing liquid filament that eventually fragments.

Further increases in Weber number ($100 \leq We < 350$) lead to sheet thinning or shear breakup, characterized by the droplet stretching into a thin sheet or ligament that subsequently disintegrates. At very high Weber numbers ($We \geq 350$), the droplet undergoes catastrophic breakup, where it rapidly disintegrates into a fine mist due to intense aerodynamic forces.^[5] These well-defined regimes are crucial for understanding atomization mechanisms and play a significant role in optimizing various applications, including fuel injection, spray drying, and agricultural spraying. The breakup regimes corresponding to different Weber number ranges for ethanol are summarized in the table 2.2 below:

We Range	Breakup Regime	Description
$We < 12$	Vibrational	Droplet oscillates without breaking, retains its original shape.
$12 \leq We < 50$	Bag Breakup	A central bag inflates and bursts, producing secondary droplets.
$50 \leq We < 100$	Bag-Stamen Breakup	A bag with trailing filament forms and then breaks into fragments.
$100 \leq We < 350$	Sheet Thinning / Shear	Droplet stretches into a sheet and disintegrates gradually.
$We \geq 350$	Catastrophic Breakup	Droplet shatters into fine spray due to intense aerodynamic forces.

Table 2.2: Breakup regimes of ethanol droplets at different Weber number ranges

The table 2.3 provides a comparative overview of droplet breakup regimes across different Newtonian fluids—water, ethanol, 70% glycerol solution, and oil—based on their corresponding Weber number (We) ranges. For both water and ethanol, which possess relatively low viscosity and surface tension, the transition from no breakup to bag breakup occurs at $We \approx 10$, with subsequent regimes such as bag-stamen, multibag, and shear stripping following at $We \approx 30$, 60, and 80, respectively. This indicates a classic progression of aerodynamic breakup modes typical of low-viscosity Newtonian fluids. ^[1,5,10]

Fluid Type	No Breakup	Bag Breakup	Bag-Stamen	Multi bag	Shear Stripping
Water	$We < 10$	$10 \leq We < 15$	$16 \leq We < 22$	$25 \leq We < 90$	$We \geq 90$
Ethanol	$We < 12$	$12 \leq We < 15$	$15 \leq We < 40$	$40 \leq We < 95$	$We \geq 95$
Glycerol 70%	$We < 12$	$12 \leq We \leq 18$	$19 \leq We < 45$	$45 \leq We < 100$	$We \geq 100$
Diesel oil	$We < 12$	$12 \leq We < 35$	$35 \leq We < 80$	$80 \leq We < 170$	$We \geq 170$

Table 2.3: Breakup regimes for different Newtonian fluids as a function of Weber number (We). ^[4,5]

In contrast, the 70% glycerol solution, due to its significantly higher viscosity, requires a higher threshold for each breakup regime. Bag breakup initiates only beyond $We \approx 12$, while bag-stamen and multibag transitions occur within a broader range ($We \approx 19$ to 100) compared to water or ethanol. Notably, **shear stripping begins at $We \approx 100$** , indicating a delayed but rapid fragmentation once inertial forces overcome viscous damping.

Diesel oil, a moderately viscous Newtonian fluid, shows a **delayed onset of breakup** compared to water or ethanol. **No breakup persists until $We \approx 12$** , after which **bag breakup occurs from $We = 12$ to 35**, followed by **bag-stamen breakup between $We = 35$ and 80**. **Multibag breakup dominates from $We = 80$ to 170**,

and **shear stripping initiates only at $We \geq 170$** , indicating a strong resistance to aerodynamic fragmentation. This behavior aligns with the rheological characteristics of diesel oil, where higher viscosity and lower surface tension moderate early deformation and breakup.

Overall, the breakup behavior is strongly influenced by fluid viscosity and surface tension, with higher values **shifting the onset of breakup regimes to higher Weber numbers**. This comparison, reinforced by the tabulated data, underscores the critical role of fluid properties in dictating aerodynamic breakup mechanisms.

The breakup of Newtonian fluid droplets has been extensively studied through the lens of classical hydrodynamic instabilities, primarily Rayleigh-Taylor and Kelvin-Helmholtz mechanisms.^[13] In Rayleigh-Taylor instability, breakup occurs when a denser fluid is accelerated into a lighter one, leading to interfacial perturbations that grow and cause droplet deformation and eventual fragmentation. This is especially relevant in bag and bag-stamen regimes, where internal pressure differences drive the formation of thin films and ligaments.^[13] Conversely, Kelvin-Helmholtz instability dominates in high Weber number regimes, where the velocity shear between the droplet and surrounding gas promotes wave growth on the droplet surface, leading to surface stripping and fine droplet generation. These instabilities underpin the transition between different breakup modes observed in Newtonian fluids, such as water or ethanol, and provide a theoretical basis for predicting droplet behavior in atomization processes, sprays, and fluid-structure interactions.

2.2 Property of non-newtonian fluid

Non-Newtonian fluids exhibit complex rheological behavior, where viscosity is not constant but varies with shear rate, time, or both. Key fluid properties influencing droplet formation include shear-thinning or shear-thickening behavior, yield stress, viscoelasticity, and extensional viscosity. These properties significantly modify the droplet deformation, breakup, and secondary atomization mechanisms compared to Newtonian fluids.^[14]

- **Shear-Thinning:** In shear-thinning fluids (e.g., many polymer solutions or gels), viscosity decreases with increasing shear rate, which can delay breakup and result in more elongated droplets in early regimes (like vibrational or bag breakup). In contrast, shear-thickening fluids resist deformation more under high shear, suppressing surface instabilities and often delaying the transition to finer breakup modes.
- **Yield Stress:** Yield-stress fluids (e.g., concentrated suspensions, gels) do not flow

until a critical stress is applied. This suppresses the onset of Rayleigh-Taylor or bag-type instabilities, resulting in stable or partially deformed droplets at Weber numbers where Newtonian fluids would already break up. Bag and bag-stamen modes are less likely, and breakup may only occur through large external forces or high Weber numbers, often resembling "chunky" or fragmented patterns rather than smooth droplet breakup.^[14]

- **Viscoelasticity:** Many non-Newtonian fluids exhibit both viscous and elastic characteristics. Elastic stresses can resist surface deformation, dampening Kelvin-Helmholtz instabilities and delaying or suppressing shear-stripping breakup. Additionally, filament formation and "beads-on-a-string" morphology are commonly observed due to the elastic recoil of stretched fluid threads, especially in ligament-mediated breakup.
- **Extensional Viscosity:** Non-Newtonian fluids often exhibit significantly different resistance to stretching compared to shear. High extensional viscosity slows necking and ligament thinning, promoting longer lifetimes of filaments and sometimes preventing clean pinch-off, resulting in non-uniform droplet sizes and satellite droplets.^[14]

Non-Newtonian fluid properties act to stabilize the droplet and shift breakup regime thresholds to higher Weber numbers. These effects must be carefully accounted for in spray applications, inkjet printing, and drug delivery systems, where controlled atomization is critical.

The ethanol-HPMC (Hydroxypropyl Methylcellulose) and water gel systems are selected for droplet breakup studies primarily to investigate the effects of non-Newtonian rheology—especially yield stress, viscoelasticity, and shear-thinning behavior—on atomization and breakup dynamics.

HPMC, a commonly used polymer, when mixed with ethanol and water, forms a structured gel-like fluid that mimics gelled propellants, biofluids, or pharmaceutical sprays, where controlled breakup and droplet formation are critical. The ethanol component reduces the surface tension and adjusts the volatility, making the system suitable for atomization. Meanwhile, HPMC provides viscoelasticity and increases extensional viscosity, which helps resist droplet deformation, stabilizes filaments, and alters the breakup pathway—delaying transition into bag or shear stripping regimes and often leading to beads-on-string structures.^[15]

Similarly, water gels, formed by mixing water with gelling agents (like carbopol or xanthan gum), allow controlled tuning of yield stress and viscosity. These fluids are useful for

studying how resistance to initial deformation (due to yield stress) influences early-stage breakup or suppresses it altogether. They serve as a model for many real-world applications such as gelled fuels, fire retardants, or drug delivery sprays, where the atomization behavior must be tailored.

In essence, the ethanol-HPMC and water gel systems enable researchers to study complex breakup mechanisms beyond what is seen in Newtonian fluids and provide a foundation for engineering advanced spray systems where fluid rheology can be leveraged to control droplet size, distribution, and stability.

2.3 Aerodynamic breakup of the droplet

The **characteristic time** τ or t^* is a representative timescale used to describe the transient dynamics of multiphase flows, such as droplet impact, deformation, and atomization. It is defined as:

$$\tau = \frac{d_0}{U_0} \sqrt{\frac{\rho_l}{\rho_g}}$$

where:

- d_0 is the initial diameter of the droplet,
- U_0 is the characteristic (or impact) velocity,
- ρ_l is the density of the liquid,
- ρ_g is the density of the surrounding gas.

The term $\frac{d_0}{U_0}$ represents the convective timescale, while the square root term accounts for the density contrast between the liquid and gas phases. A higher liquid-to-gas density ratio results in a longer characteristic time, reflecting the dominant inertia of the liquid phase. This parameter is essential in analyzing and comparing unsteady phenomena in fluid systems.

Chou and Faeth^[16] observed that during bag breakup, the distribution of the liquid volume between the bag and the rim is approximately in the ratio of 2:3. Their study also indicated that the average fragment diameters resulting from ring and bag breakup are about 30% and 40% of the initial droplet diameter, respectively. Furthermore, they reported that the cross-stream dimension of the droplet increases linearly up to the onset of bag formation. Following this, the expansion exhibits a parabolic growth pattern, which eventually transitions back to a linear regime during the rim breakup phase. The total

duration required for complete bag breakup was found to be approximately 5 to 6 times the characteristic breakup time.

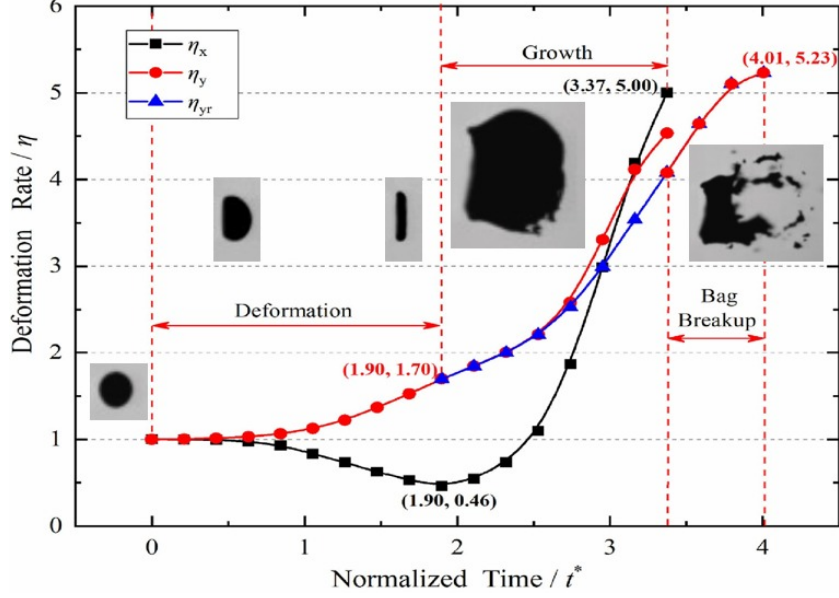


Figure 2.2: Schematic representation of stages in bag breakup^[1]

Song et al.^[17] conducted experimental investigations on microscale water droplets subjected to a continuous air jet to analyze the statistical characteristics of the breakup process. As illustrated in Figure 2.4, their results revealed that, during the bag breakup regime, the deformation along the streamwise direction (η_x) initially decreases gradually before increasing again, whereas the deformation in the transverse direction (η_y) exhibits an exponential rise until the rupture of the bag occurs. They further noted a distinct difference in the growth rates of the rim and the bag, which was attributed to the non-uniform distribution of aerodynamic forces acting separately on the expanding bag and the surrounding liquid rim.

Figure 2.2 further quantifies the deformation behavior by presenting the evolution of deformation rates in the streamwise (η_x), transverse (η_y), and total (η_T) directions as a function of normalized time t^* . The plot is divided into three distinct temporal regimes: the initial deformation phase, the intermediate growth phase, and the final bag breakup event.

During the deformation phase (up to $t^* \approx 1.9$), η_x decreases gradually to a local minimum of approximately 0.5, while η_y shows a slight increase to around 1.7, indicating a dominant transverse stretching mechanism. As the process transitions into the growth regime (from $t^* \approx 1.9$ to $t^* \approx 4.0$), both η_x and η_y increase significantly, with η_y exhibiting an

exponential growth trend. At $t^* \approx 3.4$, η_y reaches a value of about 5, while the total deformation rate η_T also rises steadily, confirming strong aerodynamic expansion of the droplet.

The onset of bag breakup occurs at $t^* \approx 4$, as indicated by a rapid rise in deformation rates and a peak value of $\eta_y \approx 5.2$, highlighting the critical instability that leads to the rupture of the bag structure. The difference in deformation behavior between the rim and the bag, particularly in their respective growth rates, is attributed to the non-uniform aerodynamic force distribution acting on the different regions of the droplet.^[18]

These observations offer valuable insights into the physical mechanisms driving droplet deformation and eventual breakup in high-speed gas flows. The initial decline in stream-wise deformation rate (η_x) suggests that the aerodynamic drag initially compresses the droplet in the direction of motion, likely due to inertia resisting the imposed external forces. Meanwhile, the gradual rise in transverse deformation (η_y) points to the development of a pressure differential across the droplet surface, initiating lateral expansion.^[18]

The exponential growth phase of η_y highlights the instability growth driven by increasing aerodynamic stress, consistent with the Rayleigh–Taylor or Kelvin–Helmholtz instability mechanisms commonly associated with bag breakup regimes. The rim’s slower growth relative to the bag is attributed to the difference in local curvature and mass concentration—rim regions are denser and experience relatively lower aerodynamic acceleration.

The sharp increase in deformation rates just before breakup marks the onset of structural failure in the droplet interface. The bag thins out and stretches under aerodynamic loading until it reaches a critical threshold, at which point rupture occurs. This behavior underscores the non-linear coupling between inertial, aerodynamic, and interfacial tension forces, and highlights the role of spatial force imbalances in governing asymmetric breakup modes such as bag-with-rim fragmentation.^[18]

The final rupture of the bag signifies the culmination of the deformation process, where the film-like structure of the bag becomes sufficiently thin and unstable under aerodynamic loading. As the internal pressure within the bag builds up due to continuous stretching, the capillary and viscous forces can no longer resist the external aerodynamic stresses. Once the local Weber number exceeds a critical threshold, the film ruptures, leading to a violent disintegration of the droplet structure.

This rupture is of particular significance because it marks the transition from coherent droplet deformation to the formation of a dispersed spray. The breakup results in

two primary components: a thin liquid film (the bag) that shatters into numerous fine droplets due to high surface area and low thickness, and a denser toroidal rim that fragments into comparatively larger droplets due to its higher inertia and mass concentration.

The formation of small droplets is primarily governed by capillary instabilities and surface tension-driven retraction at the moment of rupture. The bag's thin structure and rapid acceleration cause it to fragment into droplets with high surface-to-volume ratios, enhancing atomization efficiency. This phenomenon is critical in applications such as fuel injection and spray cooling, where finer droplet size improves mixing, evaporation, and overall system performance. Thus, understanding the dynamics of the final rupture stage provides crucial insight into droplet size distribution and spray characteristics in multiphase flow systems.

2.4 Numerical study on shear-thinning droplet atomization

In the numerical investigation conducted by Li et al.^[19], the secondary atomization behavior of shear-thinning fluids was systematically studied to understand their deformation and breakup under aerodynamic forces. The study employed a power-law rheological model to characterize shear-thinning behavior, described by the expression:

$$\mu_{\text{apparent}} = K\dot{\gamma}^{n-1} \quad (2.1)$$

where μ_{apparent} is the apparent viscosity, $\dot{\gamma}$ is the shear rate, K is the consistency index, and n is the flow behavior index. The simulations considered a range of n values from 0.4 to 1.0, and K values from 0.00569 to 26.785 Pa·s ^{n} , thereby covering a wide spectrum of shear-thinning behaviors.^[19]

Droplets with an initial diameter of 4 mm were exposed to airflow velocities ranging from 8.54 m/s to 22.59 m/s, resulting in Weber numbers (We) between 5 and 35. A modified Ohnesorge number was proposed to account for the spatially varying viscosity in shear-thinning fluids by incorporating the characteristic shear rate induced by airflow:

$$Oh = \frac{K \left(\frac{U_r \sqrt{\rho_g / \rho_l}}{D} \right)^{n-1}}{\sqrt{\rho_l D \sigma}} \quad (2.2)$$

This modified formulation allowed for a consistent comparison between Newtonian and non-Newtonian cases under similar aerodynamic conditions.

The simulations revealed that shear-thinning droplets behave significantly differently from Newtonian fluids during secondary atomization. For example, at $We = 20$ and $Oh = 0.10746$, a Newtonian droplet exhibited classic bag breakup, whereas a shear-thinning droplet with $n = 0.4$ underwent a multimode breakup.^[19] The distribution of apparent viscosity within the droplet was found to be highly non-uniform: during bag breakup, the lowest viscosity regions were near the droplet center, while in multimode breakup (e.g., at $We = 30$), low-viscosity zones migrated toward the rim, enhancing radial stretching.

The minimum apparent viscosity (μ_{\min}) inside the shear-thinning droplets was often significantly lower than the Newtonian viscosity used for comparison, and this variation directly influenced deformation patterns. Furthermore, changes in the flow index n showed non-monotonic effects on deformation metrics like cross-stream diameter and centroid velocity, indicating a complex interplay between shear rate, local viscosity, and aerodynamic force.

This study provides quantitative and mechanistic insight into how shear-thinning rheology affects droplet breakup. It emphasizes that non-Newtonian characteristics, especially viscosity gradients, can shift breakup regimes and alter deformation dynamics. Such findings are critical for the accurate modeling of processes like gel fuel injection, spray drying, and pharmaceutical coating, where fluid rheology must be precisely accounted for to predict atomization outcomes.

2.5 Regime map

Figure 2.3 shows the regime map plotting the Weber number (We) against the Ohnesorge number (Oh), identifying distinct modes of droplet deformation and breakup such as *no deformation*, *non-oscillatory deformation*, *oscillatory deformation*, *bag breakup*, *multimode breakup*, and *shear breakup*. The trends reveal critical insights:

- For **low-viscosity Newtonian fluids** (e.g., water, n-heptane) with $Oh < 0.01$, bag breakup begins at $We \approx 10$, and shear breakup occurs near $We \approx 80$.
- For **high-viscosity Newtonian fluids**, such as glycerol–water mixtures (Glycerol 84% to 99.5%) with $Oh > 0.1$, the onset of bag breakup shifts to significantly higher Weber numbers (e.g., $We > 30$ at $Oh = 0.1$, and $We > 100$ at $Oh = 1$).

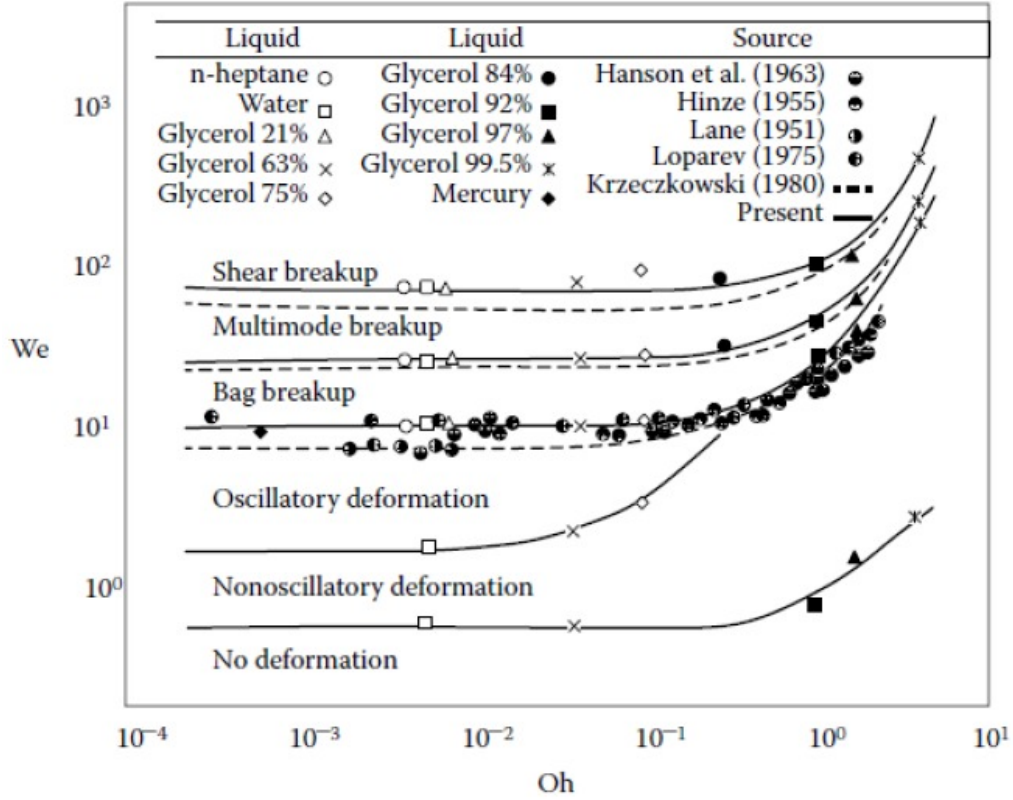


Figure 2.3: Regime map showing Weber number (We) vs Ohnesorge number (Oh) for various liquids including shear-thinning glycerol–water mixtures.^[3]

- At very high viscosity (e.g., Glycerol 99.5% with $Oh \approx 3.85$), no breakup is observed even up to $We \approx 600$, indicating strong suppression of deformation due to viscous damping.
- The oscillatory deformation regime, observed for moderate $Oh \approx 0.01$, disappears beyond $Oh \approx 0.3$, due to insufficient inertial effects to overcome viscous forces.
- The boundary between nonoscillatory deformation and bag breakup becomes highly steep in log–log space as $Oh \rightarrow 1$, reflecting the nonlinear increase in resistance to deformation.

These observations confirm that the deformation and breakup of highly viscous Newtonian droplets are strongly influenced by their viscous properties. As Oh increases, higher aerodynamic forces (i.e., greater We) are required to initiate breakup. This makes the accurate characterization of fluid viscosity essential in spray systems involving concentrated Newtonian liquids such as glycerol–water mixtures.

2.6 Summary

The review of past studies reveals that significant progress has been made in understanding the behavior of Non-Newtonian fluids, particularly in relation to their complex rheological properties and applications in various engineering processes. However, several critical gaps remain. Limited studies have focused on specific types of Non-Newtonian fluids, especially those with unique yield-stress or viscoelastic characteristics. Existing theoretical models often fall short in accurately capturing viscoelastic effects, highlighting the need for more comprehensive and physically consistent formulations. Additionally, there is a noticeable lack of experimental data under specific flow and impact conditions, which hinders model validation and further advancement in the field. Addressing these gaps is essential for developing a deeper and more predictive understanding of Non-Newtonian fluid dynamics.

Chapter 3

EXPERIMENTAL SETUP

In the experimental setup, a single liquid droplet is introduced into a horizontally directed airflow emerging from a nozzle with an exit diameter of 30 mm, as illustrated in Figure 3.1. The airflow is sourced from a high-capacity compressed air reservoir, which is interfaced with the experimental section via a pneumatic conduit. A pressure-regulating valve is integrated into the supply line to modulate and stabilize the downstream pressure, thereby maintaining consistent operating conditions within the test section. Furthermore, a mass flow controller is employed downstream of the valve to fine-tune the volumetric flow rate of air through the nozzle. This configuration enables precise manipulation of the exit velocity, ensuring reproducibility and control over aerodynamic conditions during the droplet interaction studies.

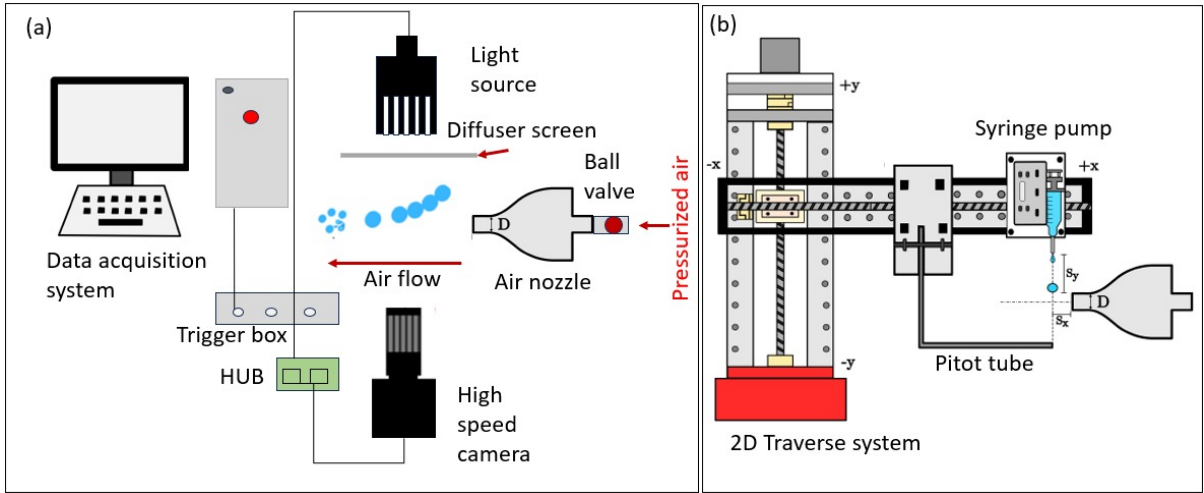


Figure 3.1: Schematic diagram of the experimental setup.

The droplet generation mechanism involves the controlled infusion of liquid at a flow rate of approximately $30\mu L/min$ through a fine-gauge needle, facilitated by a syringe pump. This pump is mounted on a vertically adjustable rail system, allowing for precise control over the release height and, by extension, the initial kinematic conditions of the droplet. The droplet is introduced into the flow field at an axial offset of roughly 10 mm downstream from the nozzle exit.

To analyze the breakup phenomena, a high-speed imaging system (IDT) is employed, with its optical axis oriented orthogonally to both the freestream direction and the droplet's trajectory. Visualization is achieved using a shadowgraphy technique, wherein a pulsed light source—operating in strobe mode with a pulse duration of $2\mu s$ is synchronized with

the high-speed camera to reduce motion blur during image capture. The camera records at 3400 fps with an exposure time of $50\ \mu s$, spanning an image resolution of 1024×508 pixels. A 150 mm fixed focal length macro lens is mounted on the camera, yielding a spatial resolution of approximately 13.1 pixels per millimeter across the field of view.

Prior to commencing the experiment, all instrumentation is meticulously aligned to ensure optimal functionality. The syringe assembly, containing the test fluid, along with the Pitot or Pitot-static tube, is mounted on a precision traverse system. This setup enables controlled bidirectional movement in the horizontal (x) and vertical (y) axes, facilitating accurate positioning of both components. The Pitot tube serves to quantify the local airflow velocity exiting the nozzle.

Using the traverse mechanism, the syringe is aligned such that the droplet is released precisely along the nozzle centerline, from a fixed vertical height of 130 mm. The droplet formation process is recorded using a high-speed imaging system coupled with a synchronized strobe light. Both the camera and illumination system are interfaced with a computer, where dedicated imaging software is employed to configure acquisition parameters, ensuring high-resolution capture of the droplet dynamics. The recorded frames are subsequently analyzed using ImageJ, an open-source image processing platform, to extract quantitative information relevant to the droplet formation and deformation processes.

3.1 Preparation of gel

In the current experimental study, a non-metallized ethanol-based gel fuel incorporating an organic gellant is employed as the working fluid. The gel formulation consists of three principal constituents: (1) research-grade ethanol (purity: 99.8%) functioning as the primary fuel, (2) Hydroxypropyl Methyl Cellulose (HPMC), a high-molecular-weight polymer serving as the organic gellant (OG), and (3) double-distilled water, which acts as the dispersion medium for the gellant. All reagents were procured from MSB Chemical Ltd. (Labnol). The specific compositions of the prepared fuel blends are outlined in Table 3.1, with the gellant loading rate (GLR) systematically varied between 3 wt.% to 5 wt.% to examine its influence on fuel rheology and atomization behavior.^[6]

An essential consideration in gel propellant formulation is the optimization of fuel content while ensuring the structural integrity and stability of the gel matrix. Within the scope of the present three-component system, the organic gellant (OG) concentration exhibits

a critical window, with 3 wt.% identified as the lower threshold for gel formation and 6 wt.% as the upper limit beyond which phase instability may occur.

The ethanol-based gel was synthesized through a systematic three-stage protocol. Initially, the required quantity of OG was dispersed in ethanol and manually agitated for approximately two minutes at ambient conditions to facilitate preliminary mixing. In the second step, deionized water was incrementally introduced to initiate gelation, followed by mechanical stirring using a laboratory-grade, three-blade impeller operating at 500 rpm for an additional two minutes to ensure homogeneity. The resulting mixture was subsequently allowed to rest undisturbed for 48 hours at room temperature. This resting period is crucial for the maturation of the gel microstructure and enables the assessment of its temporal stability, particularly with respect to phase separation and sedimentation.^[6]

Fuel Sample	Research Grade Ethanol (C_2H_5OH) %	De-ionized Water (H_2O) %	Hydroxypropyl Methyl Cellulose (HPMC) %
HPMC 3	82%	15%	3%
HPMC 4	81%	15%	4%
HPMC 5	85%	10%	5%

Table 3.1: Ethanol-HPMC composition (in % weight).^[6]

3.2 Rheological properties of gel

3.2.1 Shear thinning

In our experiment, we investigated the bag breakup phenomenon using gels composed primarily of ethanol, with hydroxypropyl methylcellulose (HPMC) and water added to facilitate gel formation. Three gel samples were prepared with HPMC concentrations of 3%, 4%, and 5% by weight, while maintaining a water content of 10-15% by weight across all samples. Since HPMC is not readily soluble in ethanol, the addition of water was essential to ensure the complete dissolution of HPMC in the ethanol medium.

Rheological testing was conducted using a concentric cylinder rheometer at a constant temperature of 25°C to evaluate the flow behavior of the gels. The viscosity versus shear rate profiles revealed that all three samples exhibited **shear-thinning behavior**, a characteristic trait of non-Newtonian fluids. Specifically, the viscosity of each gel decreased with increasing shear rate, followed by a plateau at higher shear rates, indicating pseudo-plastic flow behavior.

- **3% HPMC sample (S1):** The viscosity decreased rapidly with increasing shear rate and eventually stabilized, showing classic shear-thinning characteristics.
- **4% HPMC sample (S2):** The initial viscosity was higher than that of the 3% sample, reflecting increased resistance to deformation due to higher polymer content. It exhibited a similar shear-thinning trend, though the plateau region was reached at a slightly higher shear rate.
- **5% HPMC sample (S3):** The gel was noticeably more viscous at low shear rates, and while it also exhibited shear-thinning behavior, the overall magnitude of viscosity remained significantly higher across the shear rate range. The plateau region in this case was more gradual, indicating stronger internal structural resistance.

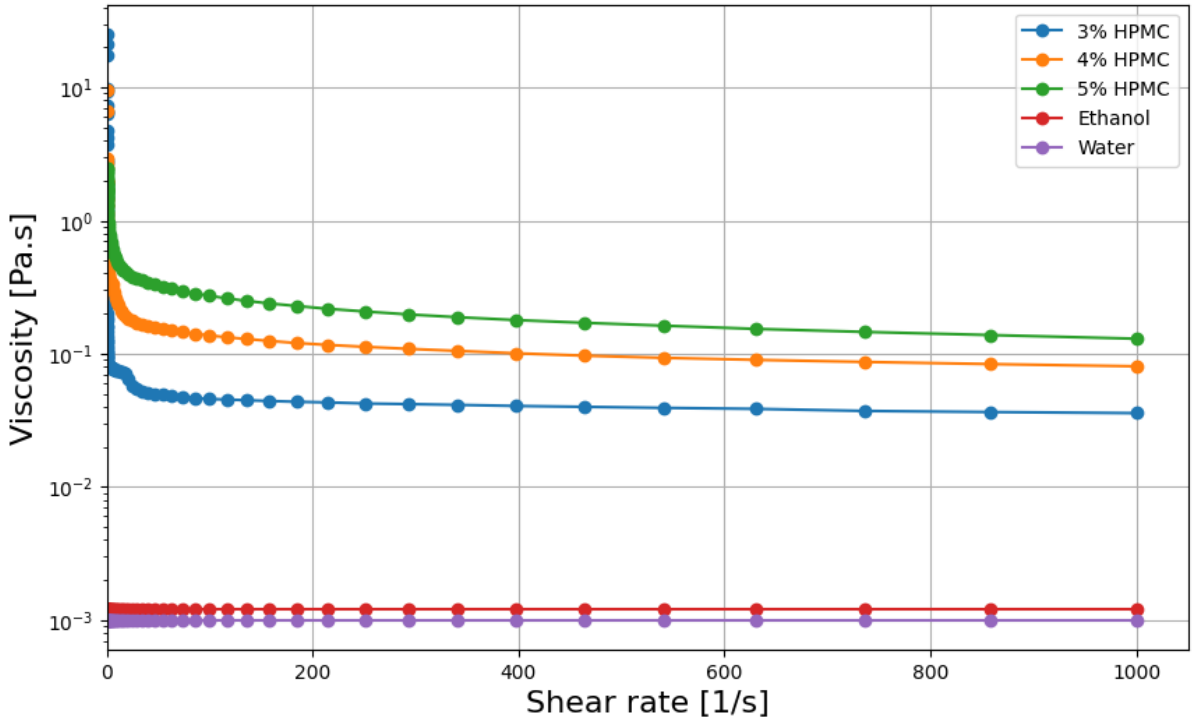


Figure 3.2: Schematic diagram of the experimental setup.

Rheological testing was performed using an Anton Paar rheometer equipped with a CP-15 circular plate geometry, set at a 15° angle, and maintained at a constant temperature of 25°C to evaluate the flow behavior of the gels. The viscosity versus shear rate profiles revealed that all three samples exhibited shear-thinning behavior, a characteristic trait of non-Newtonian fluids. Specifically, the viscosity of each gel decreased with increasing shear rate, followed by a plateau at higher shear rates, indicating pseudoplastic flow behavior.

3.2.2 Visco-elasticity

We define t_c as a fitting parameter from eqn (1), applied to the thinning process of ethanol gel within the Newtonian regime. Importantly, t_c for the ethanol gel does not indicate the actual break-up moment, but rather the time point at which the neck would have broken if no polymer was present in the solution. Hence, t_c marks the transition from Newtonian behavior to the viscoelastic regime. Based on this definition, the critical neck thickness at this transition is given by $h_c = h_{\min}(t_c)$.^[20,21]

Solutions do not undergo break-up at $t = t_c$ due to the presence of HPMC. Initially, these polymer chains are in a coiled state, but under increasing stress, they begin to unwind in a phenomenon known as the coil-stretch transition. Once fully unwound, the HPMC increase the solution's viscosity, inducing viscoelastic behavior. Consequently, for $t > t_c$, the thinning dynamics of the solution significantly slow, transitioning into the viscoelastic regime. The fluid neck evolves into a long filament of uniform thickness, thinning exponentially, which can be described by the expression:

$$h_{\min} \propto e^{-t/(3\lambda_R)}$$

where λ_R is the longest relaxation time of the polymer. Recent studies also indicate that the liquid interface exhibits a self-similar structure during viscoelastic thinning in solutions.^[21]

As observed from Fig. 3.3, the early-stage thinning behavior follows the relation

$$\frac{h_{\min}}{d_n} = k(t_c - t)^{2/3}$$

where d_n is the needle diameter, and k is a proportionality constant. In this case, $k = 0.07(t_c - t)^{2/3}$. Following this initial phase, the neck thickness evolves exponentially, described by

$$\frac{h_{\min}}{d_n} = Ae^{-B(t-t_c)}$$

where $A = 0.11$ and $B = 0.25$. This transition marks the change in the thinning dynamics as the system shifts from the Newtonian regime to viscoelastic behavior.^[21]

3.3 Experimental test conditions

Once all instruments are properly set, initiate the airflow through the nozzle and measure the velocity using the Pitot tube. A syringe with a needle diameter of 0.9 mm is used,

and the traverse mechanism is employed to position the needle at the center of the nozzle, which has a diameter of 30 mm. The needle is positioned 10 mm sideways from the nozzle and located 130 mm above the nozzle center.

Set the syringe pump to deliver a flow rate of 30 $\mu\text{L}/\text{min}$ and fill the syringe with the designated fluid. Activate the syringe pump to allow droplets to form and fall.

Configure the region of interest (ROI) using the camera software to capture all relevant details of droplet formation. Once the droplet interacts with the airstream, capture sequential images and measure the droplet's thickness and width in each frame until the first rupture occurs.

Finally, plot the droplet width and thickness against time to analyze the progression of the droplet deformation.

3.4 Property calculation

Density Ethanol $\rho_{\text{Ethanol}} = 789 \text{ Kg}/\text{m}^3$

Density Water $\rho_W = 1000 \text{ Kg}/\text{m}^3$

Density HPMC $\rho_{\text{HPMC}} = 1100 \text{ Kg}/\text{m}^3$

$$\rho_{\text{Mixture}} = \frac{m_{\text{Ethanol}} + m_{\text{Water}} + m_{\text{HPMC}}}{V_{\text{Ethanol}} + V_{\text{Water}} + V_{\text{HPMC}}}$$

$$m_{\text{Ethanol}} = \rho_{\text{Ethanol}} \times V_{\text{Ethanol}}, \quad m_{\text{Water}} = \rho_{\text{Water}} \times V_{\text{Water}}, \quad m_{\text{HPMC}} = \rho_{\text{HPMC}} \times V_{\text{HPMC}}$$

To calculate the density of the mixture, we consider a total mass of 100 grams, consisting of 82% ethanol, 15% water, and 3% HPMC by mass. Using the relationship between mass and volume for each component, the density of the mixture is determined by dividing the total mass by the sum of the volumes of ethanol, water, and HPMC. Based on this formulation, the calculated density of the mixture is approximately $839 \text{ kg}/\text{m}^3$.

The pendant drop method is a precise technique for measuring surface tension by analyzing the shape of a liquid drop suspended from the tip of a thin tube, in this case, with a needle diameter of 0.9 mm. A droplet is formed and stabilized by the balance of gravitational forces and surface tension. An image of the droplet is captured, and key geometric parameters such as the maximum diameter and neck width are extracted.

These measurements are used in conjunction with the Young–Laplace equation, which describes the pressure difference across the liquid’s surface.

To calculate the surface tension, the Axisymmetric Drop Shape Analysis (ADSA) method is employed to match the droplet profile to a theoretical shape. In this process, *Open-Drop* software is used to analyze the droplet’s geometry and compute surface tension. The method provides a highly accurate, non-invasive measurement suitable for various liquids, including both Newtonian and non-Newtonian fluids.

The droplet formation will be analyzed for various velocities and corresponding Weber numbers. Measurements will be taken to assess the droplet behavior under these specific conditions, allowing for a detailed investigation of the relationship between velocity, Weber number, and droplet dynamics. Based on experimental measurements, the surface tension values were found to be 0.027 N/m, 0.028 N/m, and 0.030 N/m for 3% HPMC, 4% HPMC, and 5% HPMC solutions, respectively.

Parameter	Ethanol based gel S-I
U_0	10-20
D_0	2.57 mm
We	10-40

Table 3.2: Process parameter used in the present study

The Ohnesorge number, defined as

$$Oh = \frac{\mu_{\text{eff}}}{\sqrt{\rho_l D_0 \sigma}}, \quad (3.1)$$

is commonly used in the analysis of fluid dynamics, particularly in the context of droplet formation and atomization processes. Here, the effective liquid viscosity, μ_{eff} , is given by:

$$\mu_{\text{eff}} = \frac{\tau_0}{\dot{\gamma}} + K \dot{\gamma}^{n-1}, \quad (3.2)$$

where τ_0 is the yield stress, $\dot{\gamma}$ is the shear rate, K is the consistency index, and n is the flow behavior index.

For secondary atomization, the characteristic strain rate is expressed as:

$$\dot{\gamma} = \frac{U_{\text{mix}}}{D_0}, \quad (3.3)$$

where U_{mix} is the characteristic velocity of the bulk liquid inside the droplet, and D_0 is the initial droplet diameter.

Since the kinetic energy of the surrounding airflow drives the motion of the liquid within the droplet, it is assumed that the inertia of the surrounding air is on the same order as the inertia of the liquid within the droplet. Thus, the bulk liquid velocity can be approximated as:

$$U_{\text{mix}} \approx \sqrt{\frac{\rho_a}{\rho_l}} U_0, \quad (3.4)$$

where ρ_a is the density of the surrounding air, ρ_l is the density of the liquid, and U_0 is the velocity of the surrounding airflow.

3.5 Image analysis and data processing

We will analyze droplet formation at a velocity of 15.5 m/s and systematically measure all relevant parameters associated with the droplet formation process. This will involve capturing data on droplet size, shape, and formation dynamics to evaluate the characteristics of the resulting droplets under these specific flow conditions.

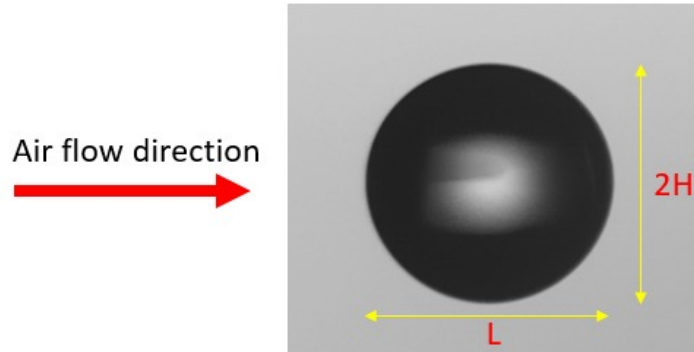


Figure 3.3: Droplet dimension

In the context of the given image, the dimension denoted by L represents the streamwise direction, corresponding to the length aligned with the airflow. The dimension $2H$ refers to the cross-stream direction, which is perpendicular to the airflow. These parameters are essential for analyzing the flow characteristics and droplet deformation under the influence of the air stream.

To calibrate the image in ImageJ software, the known scale is set based on a reference measurement. The scale is defined as 10 mm corresponding to a pixel distance of 131 pixels. By dividing the pixel count by the known distance, the scale is established as 13.1 pixels per millimeter. This calibration is then applied within ImageJ to ensure accurate measurements throughout the analysis.

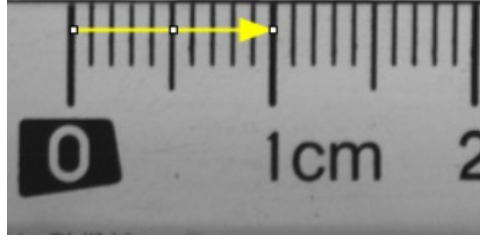


Figure 3.4: Set the scale in imagej software

Parameter	Value
Density of Air, ρ_{Air}	1.18 kg/m ³
Density of Gel, ρ_{Gel}	839 kg/m ³
Surface Tension, σ	0.027 N/m
Frame Rate	3400 fps

Table 3.3: Measured Parameters

$$T = \frac{t}{t^*}.$$

Here, the characteristic inertial timescale t^* is defined as

$$t^* = \frac{D_0}{U_g} \left(\sqrt{\frac{\rho_l}{\rho_g}} \right),$$

with D_0 being the initial droplet diameter, U_g the gas velocity, ρ_l the liquid density, and ρ_g the gas density. This non-dimensionalization of time facilitates a more effective comparison of time-dependent phenomena across different experimental conditions.

$$t^* = 6.852 \text{ ms}$$

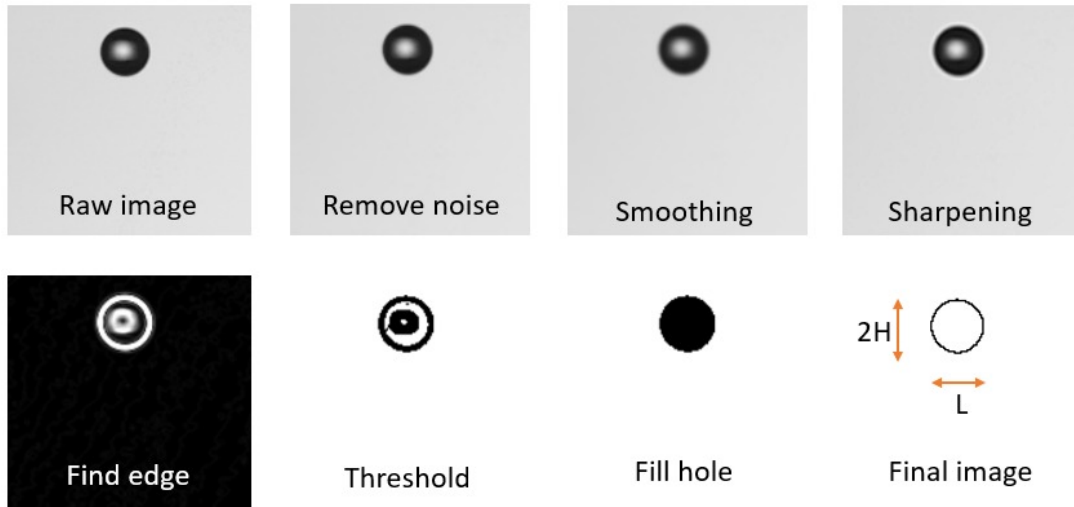


Figure 3.5: Image processing in ImageJ software

Measure the values of L (streamwise length) and $2H$ (cross-stream height) for each frame up to the point where the first breakup occurs. This specific point, where the droplet reaches its maximum dimensions before fragmenting, is referred to as the maximum width and height of the breakup, or simply the maximum breakup point.

During the bag inflation stage, a droplet exposed to significant aerodynamic forces undergoes deformation, leading to the formation of a thin, membrane-like structure referred to as the “bag.” This stretched membrane is anchored by a thicker peripheral rim at its boundary, which stabilizes the overall structure as it inflates under aerodynamic stress.

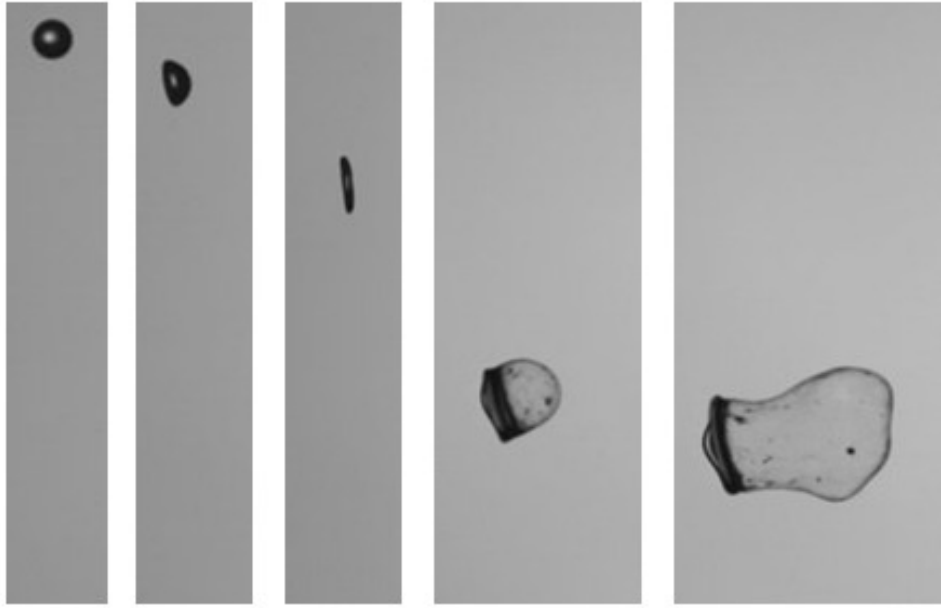


Figure 3.6: Generation of bag (We 18.4)

By plotting the graphs of L and $2H$ against T , it becomes evident that as time progresses, there is a decrease in the width along the streamwise direction, reaching a minimum value before increasing again until the point of first rupture. This behavior indicates the maximum elasticity of the gel, demonstrating its ability to deform before breaking. Such observations highlight the viscoelastic properties of the material, where the interplay between viscosity and elasticity governs the droplet’s deformation and eventual breakup.

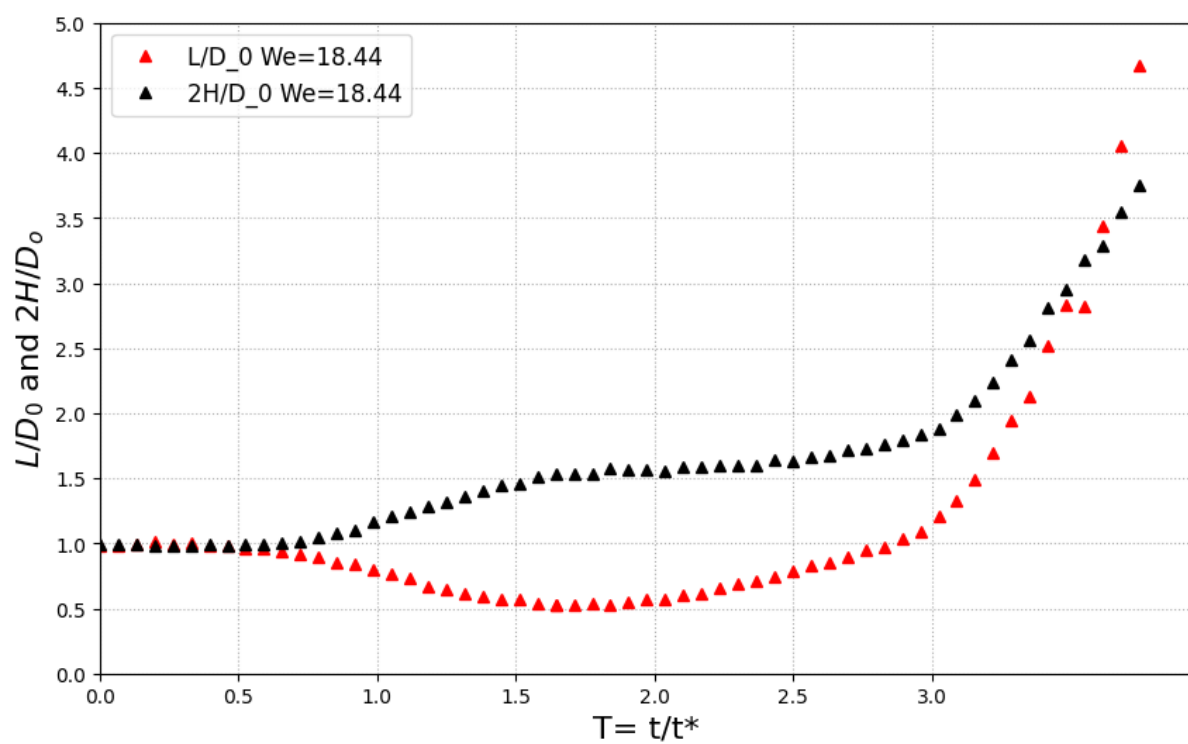


Figure 3.7: L/D_0 and $2H/D_0$ vs T (We 18.4)

Chapter 4

RESULTS AND DISCUSSION

The relaxation time (λ) of polymeric solutions was quantified using a custom-built capillary breakup extensional rheometer, employing the dripping-onto-substrate technique. In this method, a droplet is gently placed from a dispensing needle onto a pristine glass substrate, forming a liquid filament that bridges the gap between the needle tip and the substrate surface. The time evolution of the minimum neck diameter (h_{\min}) of this filament is monitored to analyze the thinning behavior of the fluid.

The initial stage of the breakup process is governed by the inertia-capillary (IC) regime, where the interplay between inertial forces and surface tension dictates the dynamics. In this regime, the neck diameter decreases gradually as inertia drives the thinning and capillary forces resist it. As the thinning progresses, the influence of the fluid's elasticity becomes pronounced—this marks the transition to the elasto-capillary (EC) regime. During this phase, the viscoelastic response of the polymeric solution becomes dominant, and the neck diameter exhibits an exponential decay with time. This behavior is attributed to the stretching of polymer chains from their initial coiled conformations, leading to elevated elastic stresses that significantly alter the breakup process.

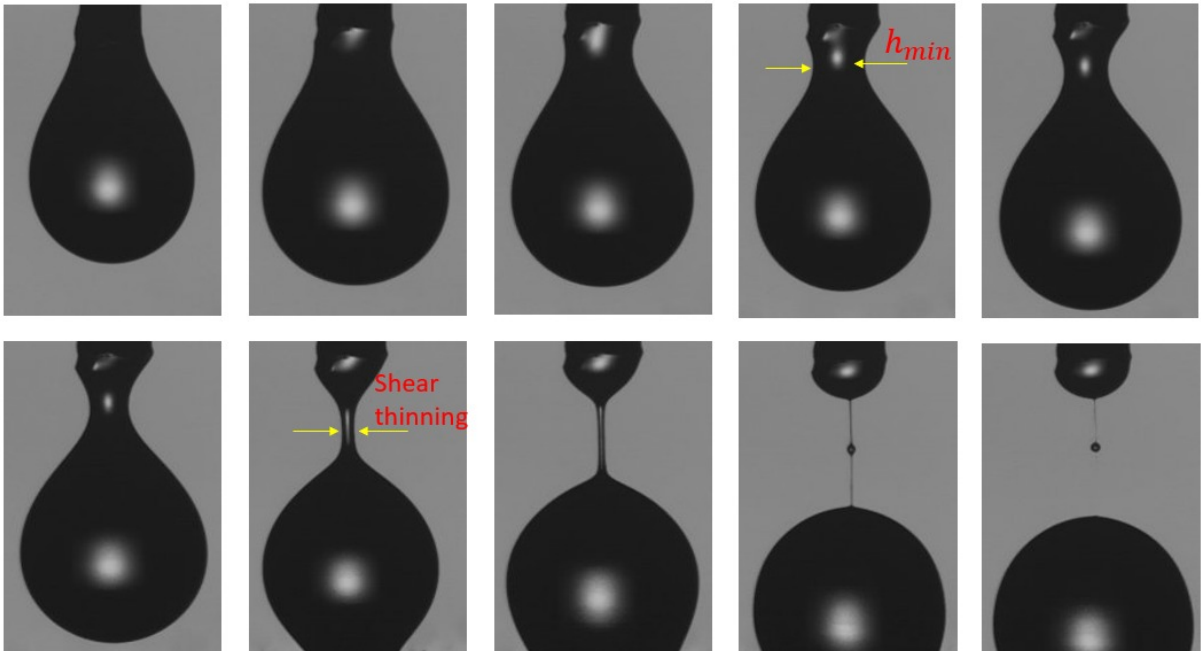


Figure 4.1: Capillary breakup elongation

As the liquid bridge continues to thin, viscous effects become increasingly dominant, with surface tension accelerating the reduction in the neck radius. Approaching the pinch-off

point—where the liquid filament attains its minimum cross-sectional area—the system nears final breakup. This stage is typically marked by the formation of a primary droplet, along with smaller satellite droplets, resulting from the interplay between inertial and capillary-driven oscillations.

The relaxation time (λ) is extracted from the exponential decay of the neck diameter observed during the elasto-capillary regime, offering quantitative insight into the viscoelastic characteristics of the polymeric solution. The complete thinning and breakup process, governed by the complex interaction of capillary, inertial, and elastic forces, reveals critical information about the extensional viscosity and the fluid's response to elongational deformation. This dynamic behavior is indicative of the fluid's non-Newtonian nature.

Figure 4.2 presents the normalized minimum neck diameter (h_{\min}/d_n) where h_{\min} is minimum thickness and d_n niddle diameter plotted against time relative to the pinch-off event ($t - t_c$) for a 3% HPMC solution. The thinning behavior transitions from a power-law regime to a distinct exponential decay, characteristic of the elasto-capillary regime.

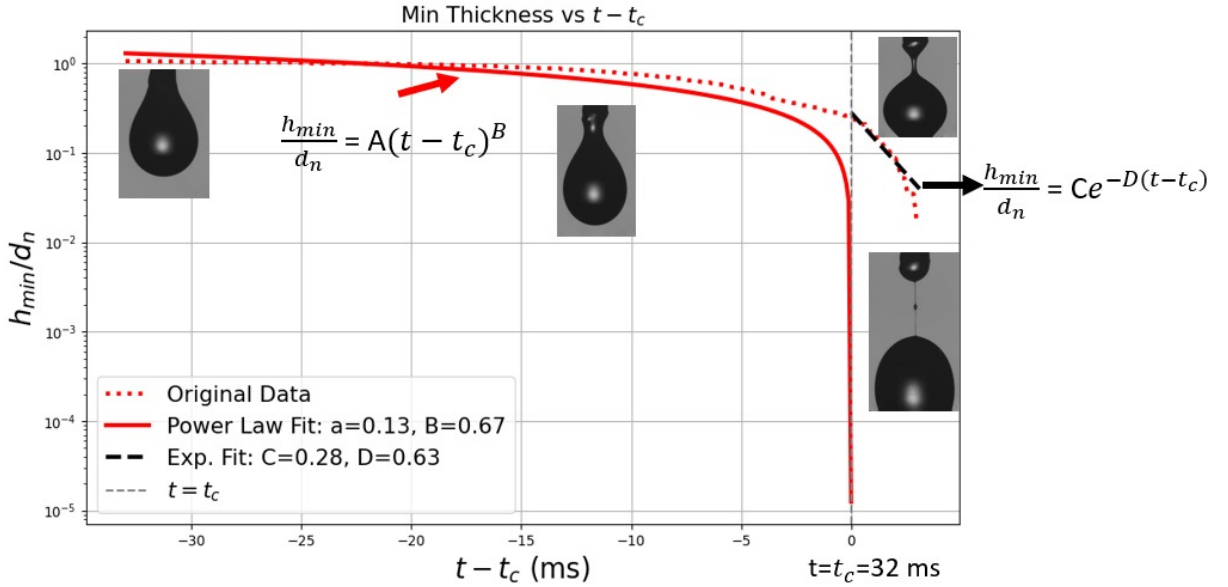


Figure 4.2: Minimum neck diameter h_{\min}/d_n as a function of time ($t - t_c$) for a 3% HPMC solution. The data is fitted with a power-law model in the inertia-capillary regime and an exponential model in the elasto-capillary regime.

In the early-time regime, the thinning follows a power-law of the form:

$$\frac{h_{\min}(t)}{d_n} = A(t - t_c)^B,$$

where $B \approx \frac{2}{3}$, consistent with the theoretical prediction for inertia-capillary driven thinning. This regime reflects a balance between inertial and surface tension forces.

As time progresses and viscoelastic effects dominate, the neck diameter follows an exponential decay:

$$\frac{h_{\min}(t)}{d_n} = C e^{-D(t-t_c)},$$

where C and D are fitting parameters. For the 3% case, the best fit yields $D = 0.63$, allowing the relaxation time to be computed as:

$$\lambda = \frac{1}{3D} = \frac{1}{3 \times 0.63} \approx 0.53 \text{ ms}.$$

This relaxation time characterizes the timescale over which the polymeric solution resists elongational deformation. For higher concentrations, enhanced elasticity results in lower decay rates and larger λ values:

- 4% HPMC: $D = 0.25 \Rightarrow \lambda = 1.33 \text{ ms}$,
- 5% HPMC: $D = 0.12 \Rightarrow \lambda \approx 2.78 \text{ ms}$.

This progression highlights the increasing viscoelastic response of the fluid with concentration and reaffirms its non-Newtonian behavior under extensional flow.

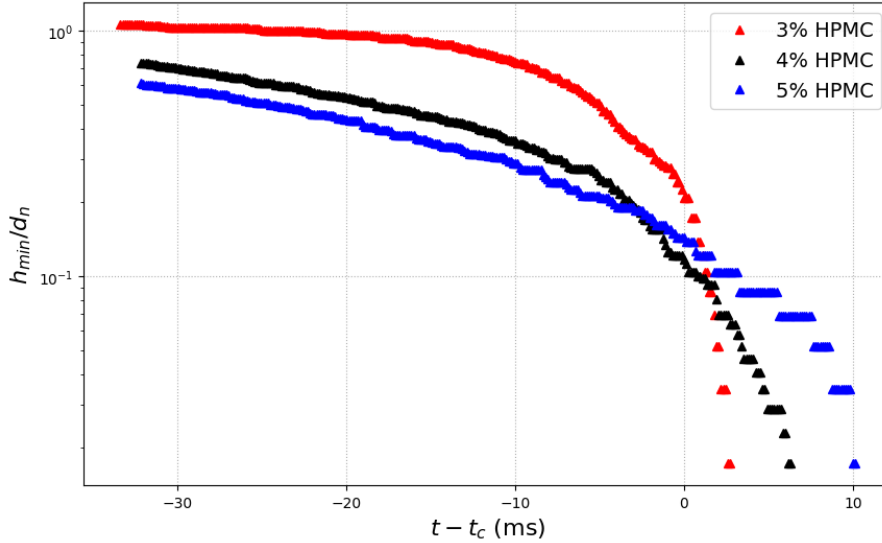


Figure 4.3: Comparison of normalized minimum neck diameter (h_{\min}/d_n) as a function of $(t - t_c)$ for 3%, 4%, and 5% HPMC solutions. The early-time behavior for all concentrations follows inertia-capillary thinning with a power-law decay ($B \approx 2/3$), while the late-time behavior shows exponential decay due to viscoelastic effects. Increasing polymer concentration leads to slower thinning and higher relaxation times, indicating stronger viscoelasticity.

To compare the effect of polymer concentration on the breakup dynamics, Figure 4.3 shows the normalized neck thinning profiles for 3%, 4%, and 5% HPMC solutions. As concentration increases, the onset of the elasto-capillary regime occurs earlier, and the rate of exponential thinning slows significantly. The corresponding decay rates D are 0.63,

0.25, and 0.12 for 3%, 4%, and 5% concentrations respectively, resulting in relaxation times of approximately 0.53 ms, 1.33 ms, and 2.78 ms. This progressive increase in λ highlights the stronger viscoelastic resistance imparted by higher polymer concentrations. These findings emphasize the pronounced non-Newtonian behavior of the fluid, with viscoelastic effects playing a dominant role in controlling the breakup dynamics under extensional flow.

4.1 Bag breakup mode

To further explain the secondary atomization dynamics, the temporal evolution of the normalized lateral extension L/D_0 was systematically analyzed, as illustrated in Fig. 4.5. The data reveal a distinct bag-type expansion behavior across all three HPMC concentrations, confirming the prevalence of the bag breakup regime. However, the degree of expansion and the underlying deformation mechanics exhibit strong dependence on both the Weber number (We) and the viscoelastic properties of the solutions.

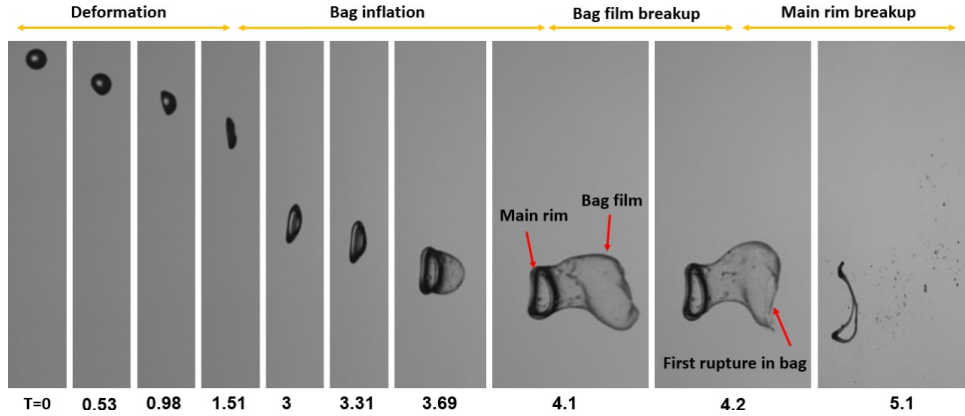


Figure 4.4: Time-resolved droplet evolution of 3% HPMC solution at $We = 23.04$, depicting key breakup stages: deformation, bag inflation, bag film breakup, and main rim breakup.

Figure 4.4 presents the time-sequenced evolution of a 3% HPMC droplet at $We = 23.04$, highlighting characteristic phases of the bag breakup process. Initially, the droplet experiences axisymmetric deformation ($T = 0$ to 1.5), followed by a notable lateral stretching that inflates a thin bag structure ($T = 3$ to 3.7). As the bag inflates, two distinct components are observed: the stretched bag film and a thicker, toroidal rim ($T = 4.1$). Eventually, the bag film undergoes rupture ($T = 4.2$), initiating fragmentation. The breakup process concludes with the disintegration of the main rim into numerous smaller droplets ($T = 5.1$). This evolution is emblematic of low-viscosity or weakly viscoelastic fluids undergoing classical bag breakup, where the dominance of inertial and aerodynamic forces drives the membrane rupture and droplet dispersion.

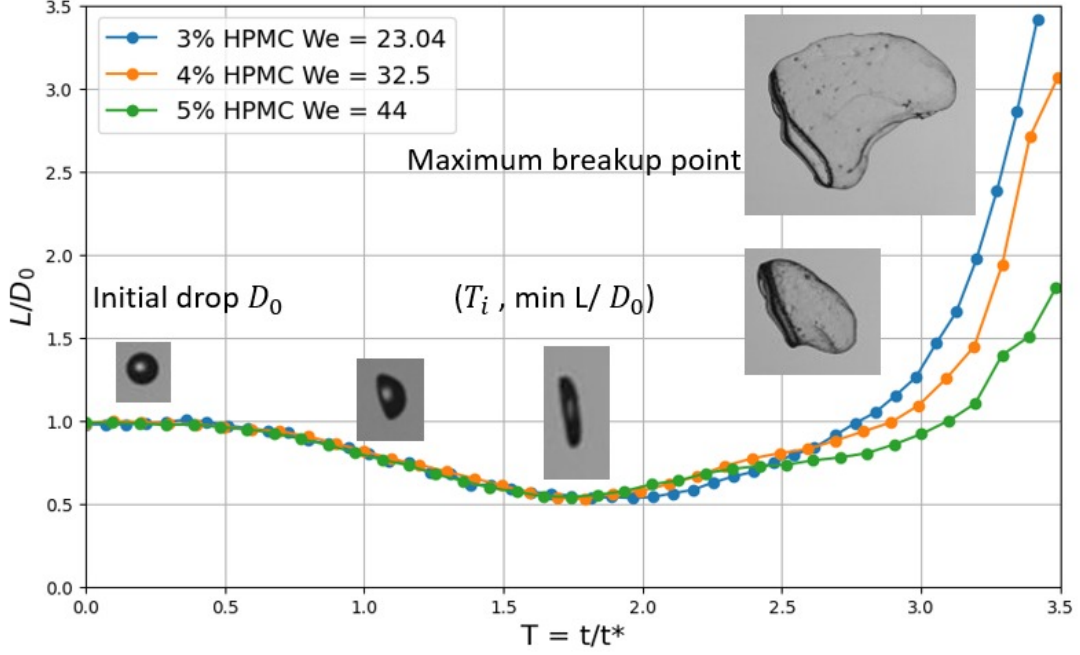


Figure 4.5: Temporal evolution of normalized lateral width L/D_0 for three different HPMC concentrations under varying Weber numbers.

For the 3% HPMC solution ($We = 23$), as quantitatively shown in Fig. 4.5, the normalized lateral width L/D_0 undergoes rapid growth beyond the dimensionless time $T > 2.5$, culminating in a maximum extension of approximately 3.4. This abrupt expansion is characteristic of a thin, unstable liquid film that undergoes significant radial stretching before catastrophic rupture—a behavior typical of Newtonian or weakly viscoelastic fluids. The absence of substantial elastic resistance allows for extensive deformation, leading to the formation of a large, fragile membrane that disintegrates into fine droplets upon bursting.

In the case of the 4% HPMC solution ($We = 32.5$), the temporal evolution of L/D_0 displays a more gradual ascent, reaching a peak value of approximately 3.5. The reduced rate of expansion, compared to the 3% case, suggests an increased resistance to deformation, attributable to the higher polymer concentration. The enhanced viscoelasticity introduces additional stresses that counteract the inertial forces driving the bag expansion, thereby moderating the lateral stretching. This results in a thicker, more resilient film that undergoes slower, more controlled thinning before eventual rupture.

The 5% HPMC solution ($We = 44$) exhibits the most constrained expansion dynamics, with L/D_0 plateauing at around 1.8—significantly lower than the other two cases. Here, the elevated polymer concentration imparts strong viscoelastic resistance, effectively suppressing large-scale film formation. The high elasticity inhibits the rapid radial stretching observed in lower-concentration solutions, leading to a more stable, less frag-

mented breakup process. Instead of forming a thin, expansive bag, the droplet deforms into a thicker, more coherent structure that resists violent disintegration. This behavior aligns with previous observations in highly viscoelastic fluids, where elastic forces dominate over inertial and capillary effects, stabilizing the intermediate deformation stages and reducing secondary droplet generation.

The observed trends underscore the critical role of viscoelasticity in modulating breakup morphology. At low polymer concentrations, the fluid behaves in a near-Newtonian manner, facilitating classical bag breakup with extensive film expansion and violent rupture. As polymer content increases, the growing elastic contribution dampens large deformations, transitioning the breakup regime toward a more restrained, stable mode. These findings highlight the delicate interplay between inertial, capillary, and elastic forces in determining the fragmentation characteristics of viscoelastic droplets, with implications for applications requiring controlled atomization, such as spray coating, fuel injection, and pharmaceutical aerosol delivery.

4.2 Bag breakup morphology and regime classification

The breakup behavior of viscoelastic droplets under aerodynamic stress is governed by a complex interplay between inertia, surface tension, viscosity, and elasticity. Table 4.1 provides a detailed classification of breakup regimes for varying concentrations of hydroxypropyl methylcellulose (HPMC), characterized over a range of Weber numbers (We). The Weber number is a key non-dimensional parameter determining the onset and type of droplet fragmentation.

Sample	No Breakup	Bag Breakup	Bag-Stamen	Multi-Bag
3% HPMC	0–11	12–24	24–30	30–40
4% HPMC	0–17	17–30	30–45	45–95
5% HPMC	0–18	18–44	–	45–96

Table 4.1: Weber number ranges corresponding to breakup regimes for different HPMC concentrations.

For the 3% HPMC solution, the breakup initiates at relatively low Weber numbers, with the classical **bag breakup** mode observed in the range $We = 12\text{--}24$. At these concentrations, the solution behaves closer to a Newtonian fluid, and inertial forces easily overcome the surface tension and low viscoelastic resistance. As We increases, the droplet undergoes further deformation leading to the **bag-stamen** regime, where a central filament forms within the bag-like membrane. This mode occurs due to localized thinning and delayed rupture in the center, a behavior sensitive to both fluid viscosity and elongational properties.

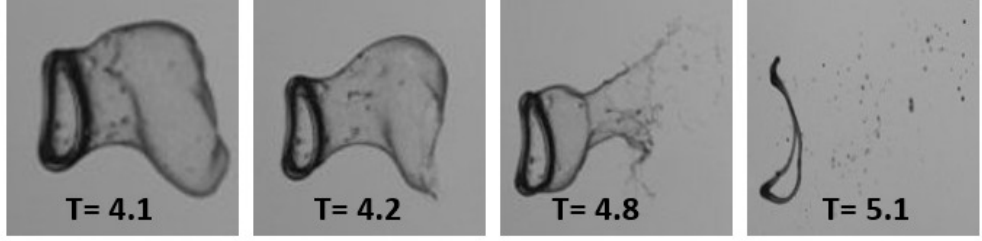
At higher Weber numbers ($We = 30\text{--}40$), the droplet enters the **multi-bag** regime. Here, the initial bag membrane bursts into multiple substructures due to increased instability. The dominance of inertial forces in this regime leads to violent fragmentation, indicating surface tension and viscosity can't maintain structural integrity.

Figure 4.8 visually demonstrates the temporal evolution of breakup regimes for the 3% HPMC sample under increasing Weber numbers. The images clearly depict the morphological transitions between bag breakup ($We = 23$), bag-stamen ($We = 30$), and multi-bag breakup ($We = 40$), reinforcing the classification summarized in Table 4.1.

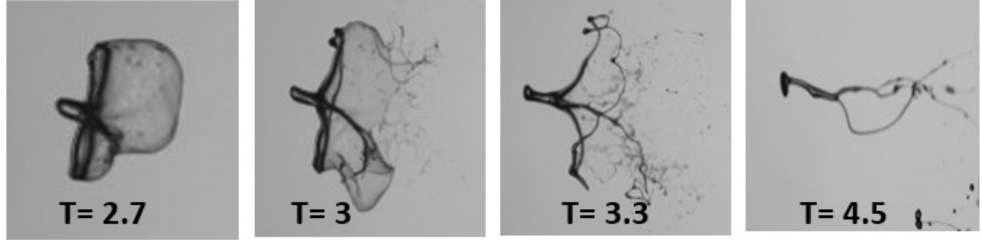
At $We = 23$, the droplet expands into a thin membrane supported by a rim, which subsequently ruptures to form fragments—a typical **bag breakup**. As We increases to 30, a central filament emerges, producing the **bag-stamen structure** due to elongational effects and delayed central rupture. At $We = 40$, the membrane becomes unstable and disintegrates into multiple sub-bags and ligaments, signifying a **multi-bag breakup**, driven by inertial dominance and elastic collapse.

This image sequence illustrates not just the qualitative breakup modes but also highlights the time scales (T values shown in milliseconds) over which these instabilities develop. It provides a compelling visualization of how the interplay between aerodynamic stretching and fluid elasticity determines the breakup dynamics.

Bag-breakup
We = 23



Bag-stamen
We = 30



Multi-bag
We = 40

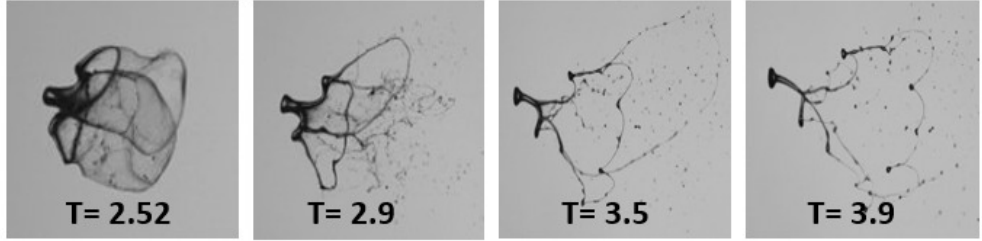


Figure 4.6: Temporal evolution of bag, bag-stamen, and multi-bag breakup for 3% HPMC droplets at different Weber numbers.

For the 4% HPMC sample, the onset of bag breakup is delayed ($We = 17\text{--}30$), suggesting increased resistance due to polymer elasticity. The **bag-stamen regime** is more extended ($We = 30\text{--}45$), implying that elastic stresses resist symmetric rupture and promote filament formation. This indicates a critical role of the Deborah number ($De = \lambda/t_{flow}$), which compares the fluid's relaxation time (λ) to the deformation timescale. Higher De delays breakup and allows time-dependent stress buildup, resulting in intermediate structures like stamens. The **multi-bag regime** initiates only beyond $We = 45$, showing that a higher inertia is needed to overcome both surface tension and viscoelastic effects.

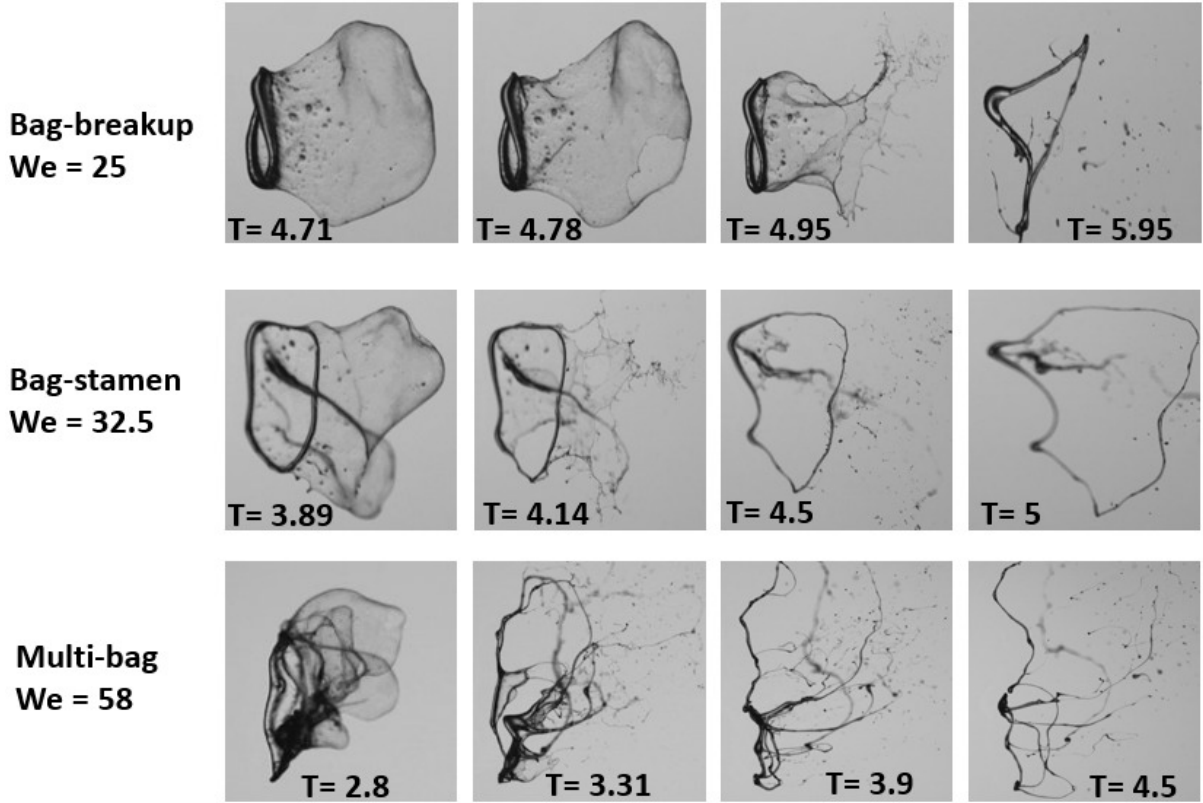
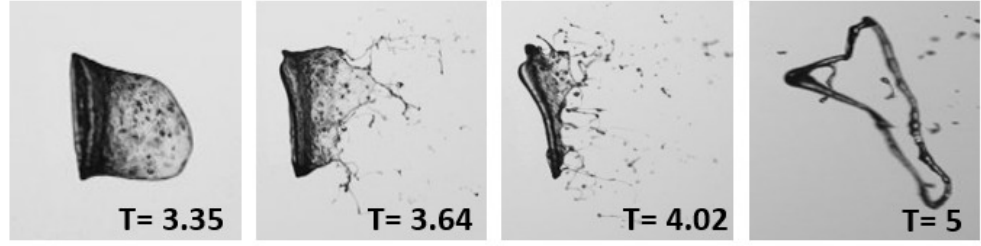


Figure 4.7: Temporal evolution of bag, bag-stamen, and multi-bag breakup for 4% HPMC droplets at different Weber numbers.

In the 5% HPMC solution, the elasticity is sufficiently dominant to suppress the bag-stamen mode entirely. The breakup transitions directly from bag ($We = 18\text{--}44$) to multi-bag ($We > 45$), with no filament formation in between. This suppression is attributed to strong extensional viscosity and elastic recoil, which stabilize the central region of the droplet and prevent asymmetric rupture. Here, both the **Ohnesorge number** (Oh) and the elastic modulus become crucial. A higher Oh leads to greater viscous damping, while elasticity provides an internal restoring force against deformation, resulting in a more cohesive response to aerodynamic stretching.

Bag-breakup
We = 44



Multi-bag
We = 93

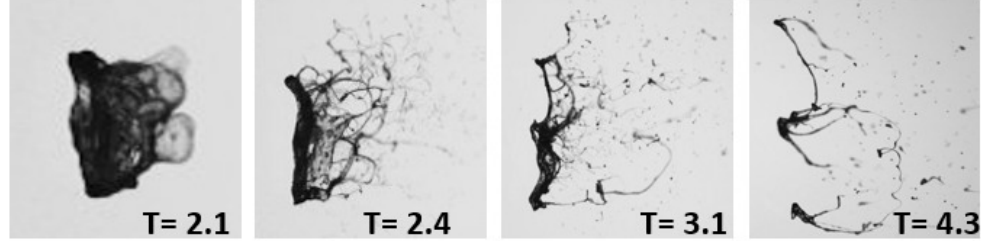


Figure 4.8: Temporal evolution of bag, bag-stamen, and multi-bag breakup for 5% HPMC droplets at different Weber numbers.

This regime mapping is critical for understanding and predicting droplet fragmentation in viscoelastic systems. The presence or absence of specific breakup modes reflects how fluid microstructure (i.e., polymer concentration and chain entanglement) controls macroscopic behavior. In practical applications like pharmaceutical sprays, agricultural atomization, or fuel injection, knowing the breakup regime enables tuning of formulation and injection parameters to achieve desired droplet sizes and spray patterns.

In summary, the regime transitions are primarily governed by:

- **Weber number (We):** determines the inertial dominance over surface tension.
- **Elastic effects (Deborah number, relaxation time):** control resistance to deformation and rupture delay.
- **Viscosity and Ohnesorge number (Oh):** influence damping and film drainage.
- **Polymer concentration:** directly affects both viscosity and elasticity, shifting regime boundaries.

Understanding how these parameters interact provides a framework for designing and optimizing viscoelastic sprays in industrial and biomedical contexts.

4.3 Regime map

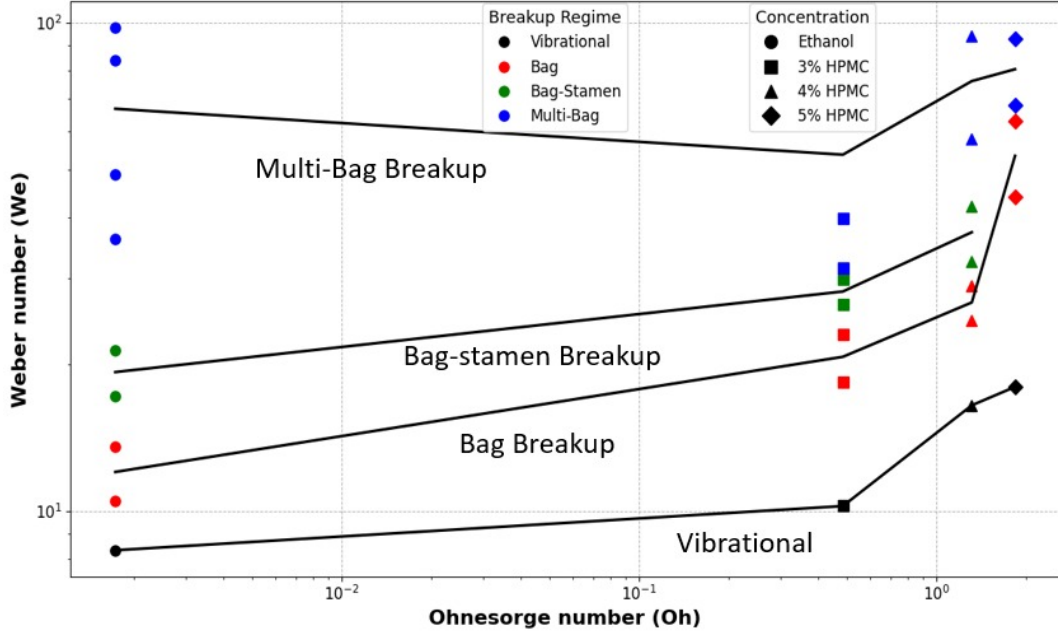


Figure 4.9: Regime map showing Weber number (We) versus Ohnesorge number (Oh) for ethanol and HPMC solutions at varying concentrations. Different breakup modes are identified across the fluid types.

The Weber number (We) versus Ohnesorge number (Oh) regime map is a widely used framework in droplet breakup studies to characterize and predict the breakup behavior of fluid droplets under aerodynamic forces. The current regime map presents experimental data for both Newtonian (ethanol) and non-Newtonian (HPMC at different concentrations) fluids, highlighting the effect of increasing viscosity on the aerodynamic breakup process.

1. **Ethanol**, with a low Ohnesorge number ($Oh < 0.05$), resides in the inertia-dominated region. It exhibits a progressive transition from vibrational to bag to multi-bag breakup with increasing Weber number. This behavior aligns with classical breakup dynamics for low-viscosity Newtonian fluids.
2. **HPMC-based fluids** show a systematic increase in Oh with concentration, indicating the growing influence of viscosity and viscoelasticity.
 - At **3% HPMC**, droplets transition through vibrational, bag, and multi-bag regimes as We increases.
 - At **4% and 5% HPMC**, the Oh is significantly higher, and the corresponding We required for breakup is also elevated. This demonstrates that *viscous*

damping delays the onset of instability and resists deformation and fragmentation.

3. The **stabilizing role of viscosity** is clearly evident. As Oh increases, droplet breakup is suppressed or occurs at higher We , shifting the breakup regime boundaries upward in the We – Oh space. Even at high We , droplets with high Oh remain in less violent regimes compared to lower viscosity fluids.
4. The **non-Newtonian nature of HPMC solutions** further contributes to the complexity, as elastic stresses may also influence the breakup characteristics in addition to viscous effects.

This regime map 4.9 provides valuable insights into the breakup behavior of droplets across a range of fluid properties. It demonstrates how increasing viscosity and complex rheology (as in gel-forming HPMC fluids) impact droplet stability under aerodynamic loading.

Such analysis is crucial for applications involving *spray combustion*, *inkjet printing*, *pharmaceutical sprays*, and *gel propellants*, where control over droplet breakup is essential for system performance. The observed regime transitions and threshold shifts help in optimizing injection and atomization parameters to achieve desired droplet sizes and breakup modes.

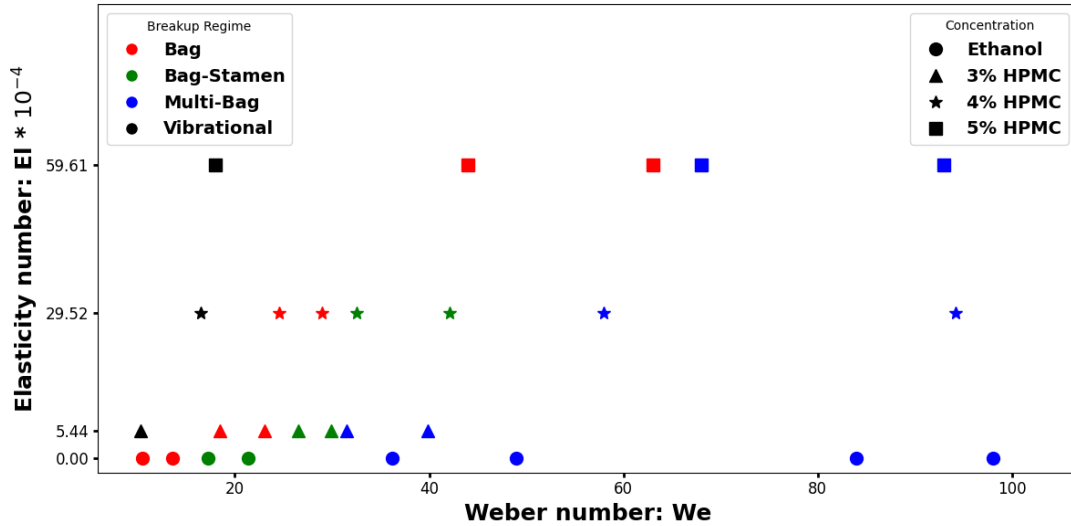


Figure 4.10: Regime map representing the variation of breakup modes with Weber number and Elasticity number for different HPMC concentrations and ethanol.

The regime map shown above illustrates the interplay between inertial and elastic effects on droplet breakup, represented in the Weber number (We) versus Elasticity number (El) space. The Weber number quantifies the ratio of inertial to surface tension forces, while

the Elasticity number characterizes the relative strength of elastic to inertial forces in viscoelastic fluids. The Elasticity number is defined as:

$$El = \frac{\lambda\mu_0}{\rho_l d_0^2} \quad (4.1)$$

where λ is the relaxation time of the fluid, μ_0 is the zero-shear viscosity, ρ_l is the liquid density, and d_0 is the initial droplet diameter. This dimensionless parameter becomes particularly important when evaluating breakup behavior in non-Newtonian or viscoelastic fluids, where internal elastic stresses resist deformation caused by aerodynamic forces.

From the regime map, it is observed that for fluids with low elasticity (such as ethanol and lower HPMC concentrations), the breakup transitions align with classical Newtonian patterns—progressing from vibrational to bag, bag-stamen, and multi-bag regimes with increasing Weber number. However, as the elasticity increases (notably in higher HPMC concentrations), the breakup transitions shift, indicating that higher elastic forces delay or modify the onset of breakup. Specifically, at high El values, more energy (i.e., higher We) is required to achieve the same breakup mode, reflecting the stabilizing role of elastic stresses.

The distribution of breakup modes across distinct regions of the We – El domain confirms that elasticity significantly alters the fragmentation dynamics. Such analysis is crucial for understanding atomization behavior in viscoelastic jets, particularly in applications like gelled fuel injection, inkjet printing, and agrochemical spray systems, where tailoring fluid elasticity can control droplet stability and breakup thresholds.

4.4 Hole rim destabilization

The first mechanism responsible for ligament formation involves the destabilization of the rim that recedes on the bag film, as depicted in Figure 4.5. When a hole forms on the bag film, it becomes unstable due to the imbalance of surface tension forces acting on the liquid edge surrounding the hole. During this stage, any elastic energy stored within the liquid phase during bag inflation contributes to the hole’s expansion. As the hole radius increases over time, the liquid from the bag film accumulates in a rim around the hole. This receding rim is subject to Rayleigh–Plateau (RP) instability, manifesting as surface corrugations that progressively develop into ligaments extending from the rim. Figure 4.5 provides a schematic of ligament formation resulting from rim destabilization, along with the associated physical variables. In this process, the wavelength of the corrugations, λ_{RP} , is governed by RP instability, while the rim thickness, d_r , at the time of

destabilization is determined by the rim's acceleration.^[?]]

$$Bo = \frac{\rho_l a_r d_r^2}{\sigma} = 1$$

Rim destabilization occurs when the local instantaneous Bond number (Bo) reaches a value of unity. At this point, the rim experiences an acceleration denoted by a_r . The criterion outlined in Equation is applicable to both Newtonian and viscoelastic liquids, although it holds true only up to a certain threshold of liquid elasticity. Beyond this limit, the elastic properties of the liquid can influence the destabilization dynamics and alter the behavior compared to purely Newtonian fluids.

$$a_r = \frac{u_r^2}{R_{bag}} \quad u_r = \sqrt{\frac{2\sigma}{\rho_l \delta}}$$

For viscoelastic liquids, the calculated value of u_r exceed that predicted by the Taylor-Culick relation, attributed to the release of elastic energy that has been stored during the bag inflation phase. This stored elastic energy enhances the overall energy available for fluid motion, resulting in higher observed velocities compared to those predicted by the traditional model. That's why we observed flutter in bag inflation.

4.5 Hole merging

The second mechanism contributing to ligament formation in non-Newtonian fluids involves the merging of two holes that develop on the bag film, as illustrated in the accompanying figure 4.6. This hole-merging phenomenon has received limited attention in the context of aerodynamic bag breakup, particularly for non-Newtonian fluids. Recent studies have begun to explore this mechanism, revealing its importance, especially under conditions of high fluid elasticity where rim destabilization is suppressed. In such cases, the merging of holes becomes the predominant mechanism for ligament formation, facilitating the transition from a stable bag film to fragmented structures as the non-Newtonian fluid flows and deforms.^[21]

As illustrated in Figure 4.5, the phenomenon of hole merging can be observed during the bag inflation process at a Weber number of 22.37. This observation highlights the dynamic interactions occurring within the bag film as it undergoes deformation, leading to the merging of holes that contribute to subsequent fragmentation.

4.6 Deformation behavior of droplets – streamwise and cross-streamwise

To understand the breakup behavior of non-Newtonian droplets during atomization, we examine both the streamwise (L/D_o) and cross-streamwise ($2H/D_o$) deformation as a function of non-dimensional time ($T = t/t^*$) for three polymer concentrations: 3%, 4%, and 5%.

Streamwise Deformation

Figure 4.11 presents the evolution of the normalized streamwise length L/D_o as a function of non-dimensional time $T = t/t^*$, across various Weber numbers and HPMC concentrations. The three subfigures capture representative cases from the *bag*, *bag-stamen*, and *multi-bag* regimes.

In the **bag regime** ($We = 14\text{--}44$), droplets experience moderate aerodynamic stresses leading to a single inflated bag-like shape. Pure ethanol ($We = 14$) shows early compression and rapid elongation. As HPMC concentration increases (up to 5%), the elongation is progressively delayed. This rightward shift in the L/D_o curve indicates that viscoelastic resistance due to the polymer retards deformation and alters the instability growth.

In the **bag-stamen regime** ($We = 21\text{--}32$), a central jet or filament forms within the inflating bag. Ethanol ($We = 21$) deforms rapidly, but 3% and 4% HPMC ($We = 29, 32$) show smoother and later elongation transitions. This behavior reflects the elastic component of the gel, which stores energy and resists immediate shape change until a critical aerodynamic stress is reached.

In the **multi-bag regime** ($We = 42\text{--}95$), higher Weber numbers generate multiple bag-like structures or lobes. Ethanol ($We = 49$) again deforms early and sharply, while HPMC-rich droplets exhibit increasing resistance and delayed deformation, with 5% HPMC ($We = 95$) showing the greatest lag. These effects arise from increased viscosity, elasticity, and yield stress behavior that inhibit aerodynamic-driven stretching.

The consistent rightward shift in deformation curves from pure ethanol to 3–5% HPMC can be attributed to:

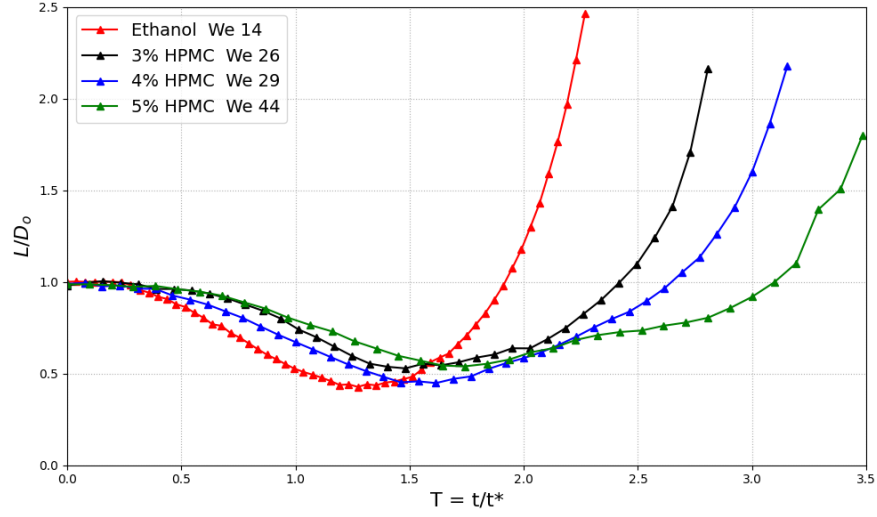
- **Higher Viscosity:** Polymer addition increases shear and extensional viscosity, reducing deformation rate.
- **Viscoelasticity:** Elastic energy storage delays the elongation response under aerodynamic force.

- **Yield Stress Threshold:** Non-Newtonian characteristics introduce a critical stress level before visible deformation initiates.
- **Structural Cohesion:** Polymer network enhances internal cohesion, delaying the onset of instability and breakup.

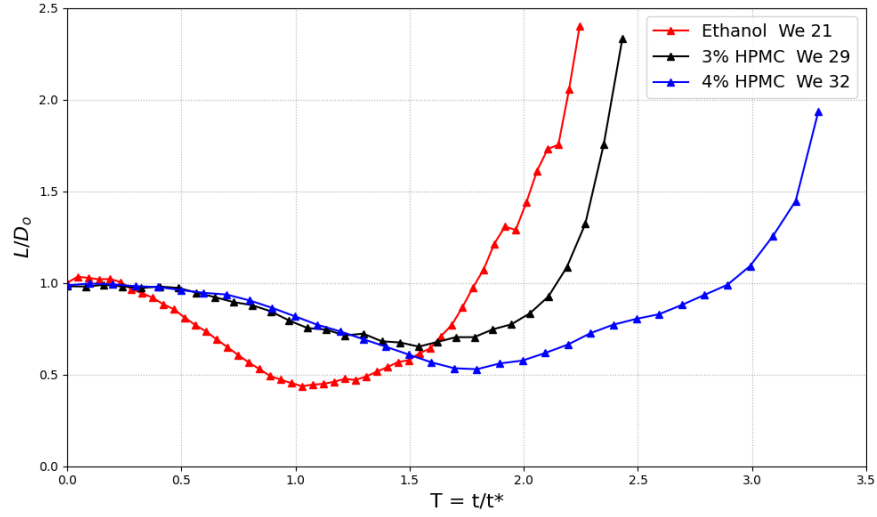
Cross-Streamwise Deformation

To complement the streamwise observations, Figure 4.12 illustrates the evolution of the cross-streamwise dimension $2H/D_o$ for three distinct breakup regimes—bag, bag-stamen, and multi-bag—at varying Weber numbers and HPMC concentrations.

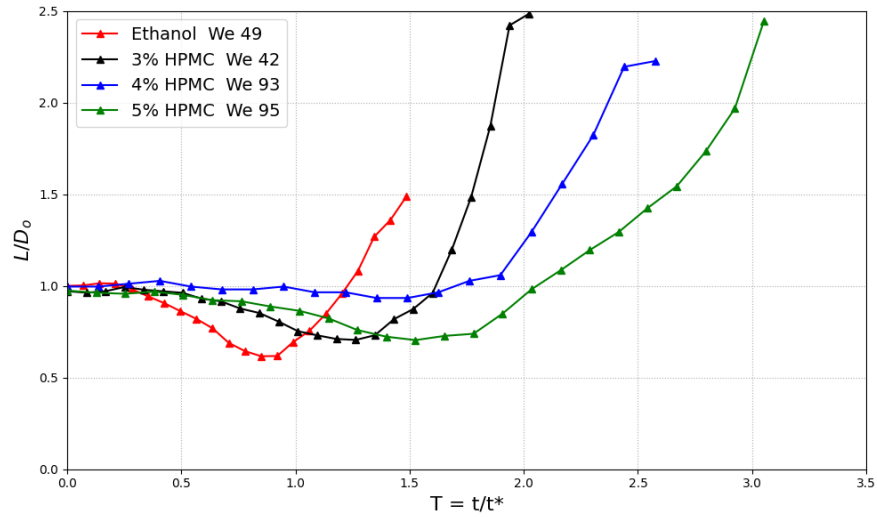
- In the **Bag regime**, a clear three-phase evolution is observed. Initially, there is a small rise in $2H/D_o$ corresponding to the initial deformation. This is followed by a moderate expansion phase, and finally, a sharp growth phase, particularly pronounced for low-viscosity ethanol and 3% HPMC solutions at lower We .
- In the **Bag-Stamen regime**, the intermediate expansion phase is more extended, and a plateau-like behavior emerges for the higher HPMC concentrations. This plateau indicates a temporary balance between aerodynamic forces and elastic/memory effects from the polymer solution, especially in 4% and 5% HPMC cases.
- In the **Multi-Bag regime**, the cross-streamwise growth initiates later but accelerates steadily. The plateau phase is still evident, but the final growth is more diffused, likely due to simultaneous inflation of multiple sub-bags altering the flow resistance across the droplet.



(a) Bag Breakup Regime

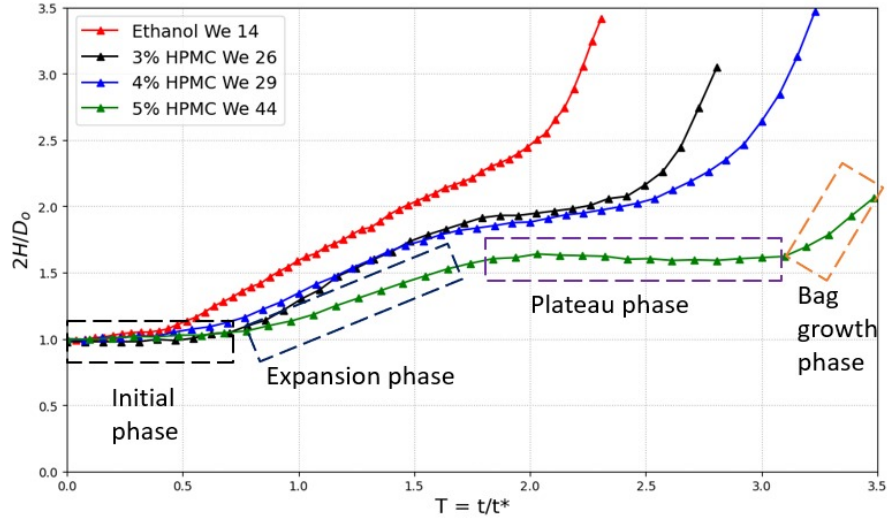


(b) Bag-Stamen Breakup Regime

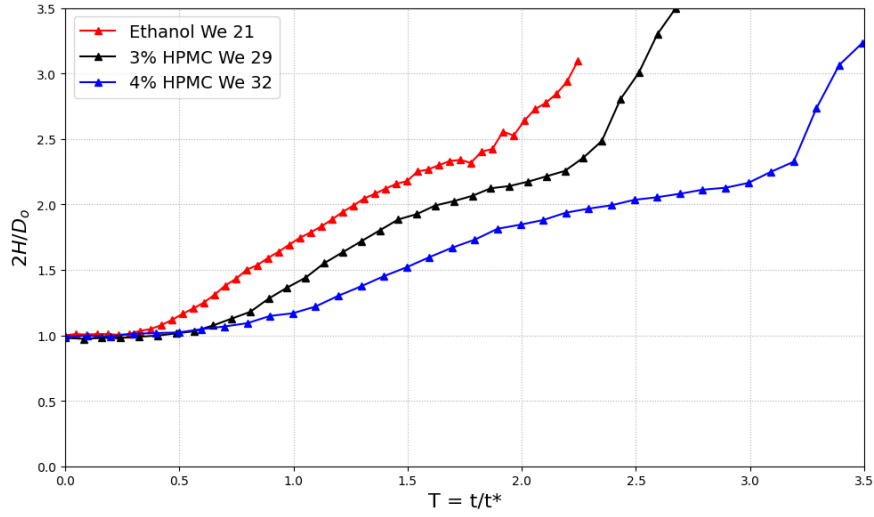


(c) Multi-Bag Breakup Regime

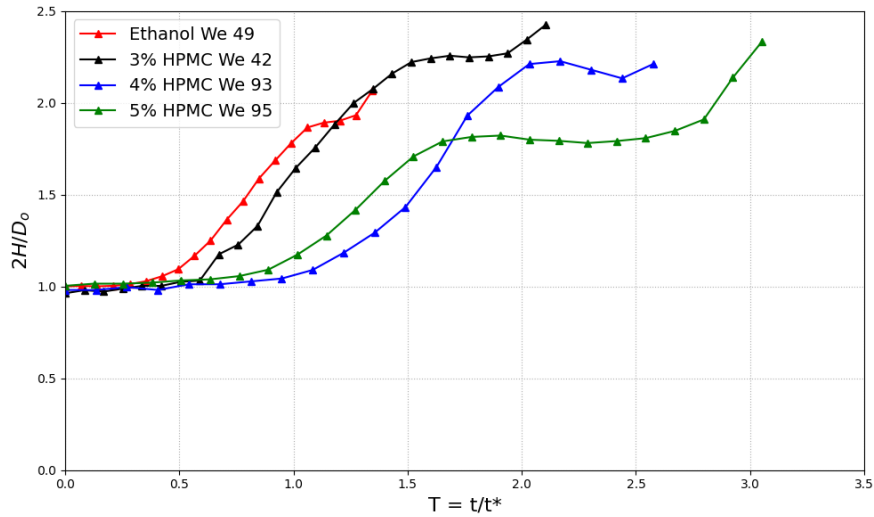
Figure 4.11: Temporal variation of L/D_o for different Weber numbers and HPMC concentrations in the streamwise direction.



(a) Bag Breakup Regime



(b) Bag-Stamen Breakup Regime



(c) Multi-Bag Breakup Regime

Figure 4.12: Temporal variation of $2H/D_o$ for different We and HPMC concentrations in the cross-streamwise direction.

4.7 Initiation time

The initiation time (T_i) is defined as the non-dimensional time elapsed from the moment the droplet enters the high-speed airflow to the onset of visible deformation. This deformation is characterized by compression in the streamwise direction and expansion in the cross-stream direction, leading to the formation of a bag-like structure. Figure 4.13 illustrates the variation of normalized initiation time $T_i = \frac{t}{t^*}$ with Weber number (We) for different fluid types, including both Newtonian and non-Newtonian fluids.

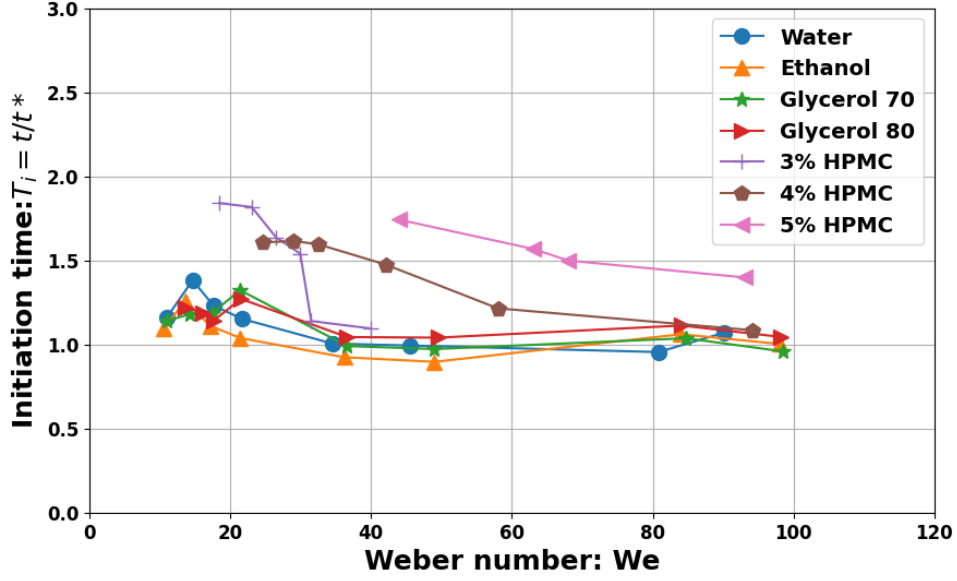


Figure 4.13: Variation of initiation time $T_i = \frac{t}{t^*}$ with Weber number for various Newtonian and non-Newtonian fluids.

For Newtonian fluids such as water, ethanol, and glycerol mixtures, the initiation time remains close to unity over a broad range of Weber numbers. This implies that the deformation leading to bag initiation is primarily governed by inertial and aerodynamic forces, with relatively low resistance from internal fluid properties.

In contrast, non-Newtonian fluids—specifically hydroxypropyl methylcellulose (HPMC) solutions at concentrations of 3%, 4%, and 5%—exhibit significantly higher initiation times. With increasing HPMC concentration, the initiation time rises from approximately 1.2 to nearly 1.9. This behavior indicates that viscoelasticity and shear-thinning properties of the fluid introduce greater resistance to deformation, thereby delaying the transition to the bag formation regime.

Moreover, while the Weber number influences droplet deformation in all cases, it is evident that in non-Newtonian fluids, internal rheological effects play a more dominant role.

Even at higher Weber numbers, HPMC solutions show consistently elevated initiation times, underscoring the influence of elastic stresses over aerodynamic forces during the initial breakup stages.

These findings suggest that non-Newtonian droplets exhibit enhanced initial stability, which may be advantageous in applications that require delayed breakup or controlled atomization.

Chapter 5

CONCLUSION

The present study systematically investigated the secondary atomization behavior of non-Newtonian fluids, particularly ethanol-based gels thickened with Hydroxypropyl Methylcellulose (HPMC) at varying concentrations (3%, 4%, and 5%). The rheological properties of the fluids, notably shear-thinning and viscoelastic behavior, were found to significantly influence the deformation, breakup initiation, and ultimate fragmentation mechanisms of droplets subjected to high-speed crossflow.

Using high-speed imaging and non-dimensional analysis, the streamwise and cross-streamwise deformation of droplets was captured and analyzed over time. For lower HPMC concentrations (3%), classic bag breakup regimes were observed at moderate Weber numbers (We), followed by bag-stamen and multibag breakup at higher We . As the concentration increased to 4% and 5%, the viscoelastic properties became more dominant, delaying the onset of breakup, reducing deformation rates, and shifting the breakup regimes to higher Weber number thresholds.

The initiation time analysis revealed that while Newtonian fluids exhibited consistent onset times for deformation (near $T_i \approx 1$), non-Newtonian droplets displayed delayed initiation, especially at higher concentrations. This behavior is attributed to the elastic resistance of the fluid, which resists initial compression and elongation. Notably, the initiation time for 5% HPMC droplets extended up to $T_i \approx 1.9$, highlighting the influence of fluid elasticity on early-stage dynamics.

Furthermore, the normalized deformation profiles (L/D_0 and $2H/D_0$) demonstrated that the degree and rate of droplet stretching reduced with increasing polymer content, confirming that viscoelastic forces suppress rapid deformation and subsequent rupture. This was evident from the plateauing of deformation in the 5% case, where classical bag formation was significantly inhibited.

Overall, the results demonstrate that the breakup behavior of non-Newtonian droplets cannot be predicted solely using conventional Weber number-based regime maps. Instead, it necessitates the inclusion of viscoelastic and extensional rheology parameters to fully describe the dynamics. These insights are critical for applications involving gelled propellants, pharmaceutical sprays, or agricultural fluids, where droplet control and stability are essential. This study provides a foundational understanding for tailoring atomization strategies in non-Newtonian fluid systems.

5.1 Future work

While this study provides significant insights into the deformation and breakup behavior of non-Newtonian droplets under aerodynamic stress, several areas remain open for further investigation.

- **Extension to Higher Polymer Concentrations:** The present experiments were limited to HPMC concentrations up to 5%. Future work could explore higher concentrations or alternative gellants to better understand the limiting behavior of viscoelastic stabilization and suppression of atomization.
- **Quantitative Modeling of Viscoelastic Breakup:** Current regime classifications rely primarily on empirical observations. Incorporating quantitative models that account for relaxation time, extensional viscosity, and elasticity number (El) would provide a more predictive framework for characterizing breakup modes.
- **Role of Drop Size and Shape:** The present study used droplets with fixed initial dimensions. A systematic study on the effect of varying initial diameter and non-spherical initial geometries could provide insights into size-dependent breakup thresholds and deformation pathways.
- **Three-Dimensional Flow Field Analysis:** Employing Particle Image Velocimetry (PIV) or numerical simulations (e.g., Volume of Fluid or Level Set methods) would help visualize and quantify internal flow patterns and stress distributions within the droplet during breakup.
- **Post-Breakup Droplet Distribution:** While this study focused on the initiation and deformation stages, an important extension would be to characterize the resulting droplet size distribution post-breakup, especially for applications where spray uniformity is critical.
- **Application-Oriented Atomization Studies:** Finally, integrating the findings into applied systems—such as fuel injectors, agricultural nozzles, or pharmaceutical spray devices—would help bridge the gap between fundamental research and engineering practice.

Addressing these directions will contribute to a more comprehensive understanding of non-Newtonian atomization and enable the design of systems that exploit fluid rheology for optimized performance.

REFERENCES

- [1] Nefeli Dimela. *Numerical simulations of primary break-up in two-phase flows*. PhD thesis, Imperial College London, 08 2017.
- [2] P.E. Charlie Young. Engineerexcel. 10 2012.
- [3] L.-P. Hsiang and G.M. Faeth. Drop deformation and breakup due to shock wave and steady disturbances. *International Journal of Multiphase Flow*, 21(4):545–560, 1995.
- [4] Daniel Guildenbecher, C. López-Rivera, and P. Sojka. Secondary atomization. *Experiments in Fluids*, 46:371–402, 03 2009.
- [5] L. P. Hsiang and Gerard M. Faeth. Drop deformation and breakup due to shock wave and steady disturbances. *International Journal of Multiphase Flow*, 21, 1994.
- [6] Ankur Miglani, Purushothaman Nandagopalan, Jerin John, and Seung Baek. Oscillatory bursting of gel fuel droplets in a reacting environment. *Scientific Reports*, 7, 06 2017.
- [7] Glen Mullineux. Non-linear least squares fitting of coefficients in the herschel–bulkley model. *Applied Mathematical Modelling*, 32(12):2538–2551, 2008.
- [8] J. O. Hinze. Fundamentals of the hydrodynamic mechanism of splitting in dispersion processes. *AIChE Journal*, 1(3):289–295, 1955.
- [9] W.-H. Chou and G.M. Faeth. Temporal properties of secondary drop breakup in the bag breakup regime. *International Journal of Multiphase Flow*, 24(6):889–912, 1998.
- [10] Krishna Kant and R. Banerjee. Study of the secondary droplet breakup mechanism and regime map of newtonian and power law fluids at high liquid–gas density ratio. *Physics of Fluids*, 34(4):043108, 04 2022.
- [11] Daniel Guildenbecher, C. López-Rivera, and P. Sojka. Secondary atomization. *Experiments in Fluids*, 46:371–402, 03 2009.
- [12] Hui Zhao, Hai-Feng Liu, Wei-Feng Li, and Jian-Liang Xu. Morphological classification of low viscosity drop bag breakup in a continuous air jet stream. *Physics of Fluids - PHYS FLUIDS*, 22, 11 2010.
- [13] Mohit Jain, R. Surya Prakash, Gaurav Tomar, and R. V. Ravikrishna. Secondary breakup of a drop at moderate weber numbers. *Proceedings of the Royal Society A: Mathematical, Physical and Engineering Sciences*, 471(2177):20140930, 2015.

- [14] De S. Vrouwenvelder J.C.R. et al Finotello, G. Experimental investigation of non-newtonian droplet collisions: the role of extensional viscosity. *Exp Fluids*, 59, 113, 2018.
- [15] Janmejai Sharma, Ankur Miglani, Jerin John, Purushothaman Nandagopalan, Javed Shaikh, and Pavan Kumar Kankar. Jetting dynamics of burning gel fuel droplets. *Gels*, 8(12), 2022.
- [16] Hui Zhao, Hai-Feng Liu, Jian-Liang Xu, Wei-Feng Li, and Kuang-Fei Lin. Temporal properties of secondary drop breakup in the bag-stamen breakup regime. *Physics of Fluids*, 25(5):054102, 05 2013.
- [17] He Song, Shinan Chang, Weidong Yu, and Ke Wu. Experimental statistics of micrometer-sized water droplet deformation and breakup behavior in continuous air jet flow. *International Journal of Multiphase Flow*, 135:103529, 2021.
- [18] S Joshi and T. N. C. Anand. Droplet deformation during secondary breakup: role of liquid properties, 2022.
- [19] Yang Li, Zhikun Xu, Xiaoyun Peng, Tianyou Wang, and Zhizhao Che. Numerical simulation of secondary breakup of shear-thinning droplets. *Physics of Fluids*, 35(1):012103, 2023.
- [20] Shadi Ansari, Md Rashid, Prashant Waghmare, and David Nobes. Measurement of the flow behavior index of newtonian and shear-thinning fluids via analysis of the flow velocity characteristics in a mini-channel. *SN Applied Sciences*, 2, 11 2020.
- [21] Navin Kumar Chandra, Shubham Sharma, Saptarshi Basu, and Alope Kumar. Aerodynamic bag breakup of a polymeric droplet. *Phys. Rev. Fluids*, 9:113303, Nov 2024.